SEARCH FOR Z’ PRODUCTION IN 4 B-TAGGED JET FINAL STATES IN PROTON-PROTON COLLISIONS

A Dissertation

by

ANDREA DELGADO

Submitted to the Office of Graduate and Professional Studies of
Texas A&M University
in partial fulfillment of the requirements for the degree of

DOCTOR OF PHILOSOPY

Chair of Committee,	Ricardo Eusebi
Committee Members,	Bhaskar Dutta
	Teruki Kamon
	Charles M. Folden
Head of Department,	Grigory Rogachev

December 2019

Major Subject: Physics

ABSTRACT

The LHCb experiment has reported slight discrepancies in the ratio in which B mesons decay to muons and electrons. Some theories attempt to explain these anomalies by theorizing the existence of new particles beyond the standard model. This study performs a search for a new heavy neutral gauge boson at the LHC with the CMS experiment. This Z' boson is assumed to couple mostly to third generation fermions, specifically b-quarks. The main production channel is b-quark fusion and since the b-quark PDF's are at least 10 times lower when compared to the gluon PDF's, we take advantage of the large contribution of bottom quarks coming from gluon-splitting to Z' production. In short, a study for Z'$\rightarrow b\bar{b}$ decays is presented. The final state consists of 4 b jets, with the two extra jets coming from the initial gluon splitting. Results correspond to 35.9 fb^{-1} of proton-proton collision data recorded by the CMS detector at the LHC with a center-of-mass-energy of 13 TeV during 2016.

DEDICATION

To Elvis, Simon, and Alice

ACKNOWLEDGMENTS

I would like to thank the Texas A&M University

CONTRIBUTORS AND FUNDING SOURCES

Contributors

This work was supported by a dissertation committee consisting of Professors Ricardo Eusebi, Bhaskar Dutta, and Teruki Kamon of the Department of Physics and Astronomy and Professor Charles M. Folden of the Department of Chemistry.

All other work conducted for the dissertation was completed by the student independently.

Funding Sources

Graduate study was supported by the Texas A&M University System Louis Stokes Alliance for Minority Participation (TAMUS LSAMP) Bridge to the Doctorate (BTD) Cohort IX (2013-2015) Program National Science Foundation Award No. HRD-1249272.

NOMENCLATURE

ATLAS	A Toroidal LHC ApparatuS
BEH	Brout-Englert-Higgs
BFF	Bottom Fermion Fusion
CERN	European Center for Nuclear Research
CMS	Compact Muon Solenoid
EMCAL	Electromagnetic Calorimeter
EW	Electroweak
EWSB	Electroweak Symmetry Breaking
FCNC	Flavor-Changing Neutral-Current
GR	General Relativity
HCAL	Hadron Calorimeter
HLT	High Level Trigger
LHC	Large Hadron Collider
η	Pseudorapidity
PF	Particle Flow
p_T	Transverse Momentum
QCD	Quantum Chromodynamics
QED	Quantum Electrodynamics
QFT	Quantum Field Theory
SM	Standard Model of particle physics
VBF	Vector Boson Fusion

TABLE OF CONTENTS

LIST OF FIGURES

LIST OF TABLES

1. INTRODUCTION

In progress...

2. THEORETICAL FRAMEWORK

2.1 The Standard Model

Particle physics is the study of the fundamental constituents of matter and the forces between them. For more than 40 years these have been described by the so-called standard model of particle physics (SM), which aims to provide, at least in principle, a basis for understanding all known particle interactions. The SM currently fails to include gravity due to the difficult task of combining the quantum theory used to describe the microscopic world and the general theory of relativity. Furthermore, its theorized force carrier, the graviton hasn't been found experimentally.

The SM can be understood as arising from an underlying symmetry of the universe, which combines the theory of electroweak (EW) interactions and that of quantum chromodynamics (QCD). In mathematical terms, the SM is formed from the gauge groups $SU(3)_C \times SU(2)_L \times U(1)_{EM}$.

2.2 Structure and Particle Content

All the phenomena described by particle physics can be explained in terms of the properties and interactions of a small number of particles of four distinct types: two spin-1/2 families of fermions called leptons and quarks; one family of spin-1 bosons (called gauge bosons) which act as "force carriers", and a spin-0 particle, called the Higgs boson [13], [14]. We should note that all particles in the SM are assumed to be elementary, i.e. they do not have internal structure or excited states.

In this section, the particle content of the SM will be introduced, along with the various force carriers. In the following sections, the specifics of particle-particle interactions will be explained in detail.

2.2.1 Fermions

Fermions are elementary particles with half-integer spin. They constitute the matter content of the SM, which accounts for 12 named fermions that interact via the weak and electromagnetic force (with the exception of neutrinos). Also, they obey Fermi-Dirac statistics and the Pauli exclusion principle, meaning that no two fermions can occupy the same quantum state within a quantum

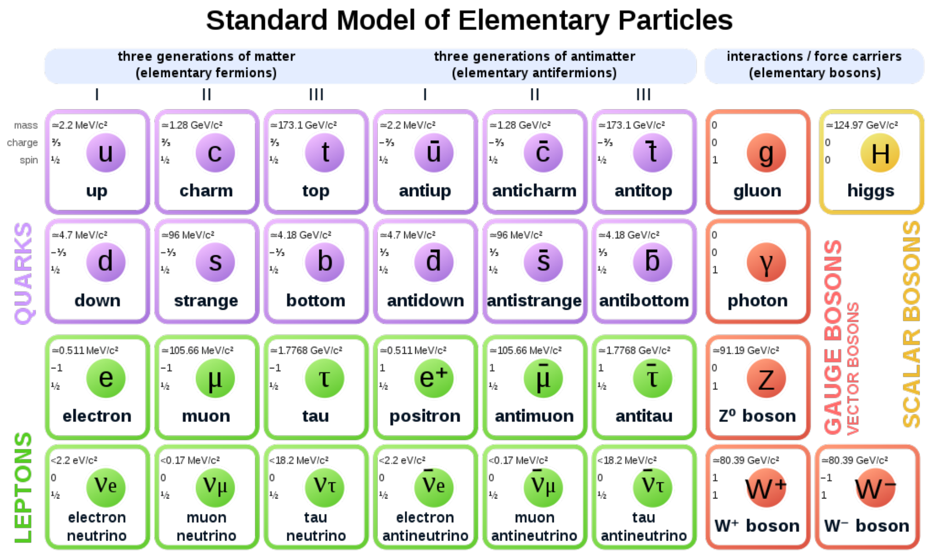

Figure 2.1: Particles of the Standard Model of particle physics. Reprinted from [1]

system simultaneously.

2.2.1.1 Leptons

There are six known leptons, and they occur in pairs called generations, which we can write as doublets:

$$\begin{pmatrix} \nu_e \\ e^- \end{pmatrix}, \begin{pmatrix} \nu_\mu \\ \mu^- \end{pmatrix}, \begin{pmatrix} \nu_\tau \\ \tau^- \end{pmatrix} \tag{2.1}$$

The three charged leptons (e^-, μ^-, τ^-) all have electric charge $Q = -q$. Associated with them are three neutral leptons, or neutrinos, called the electron neutrino, mu neutrino, and tau neutrino, respectively, all of which have very small masses. The six distinct types of leptons are also referred to as having different "flavors".

The charged leptons interact via both the electromagnetic and weak forces, whereas for neutral leptons only weak interactions have been observed. We should note that each generation of leptons has an associated quantum number. The electron number, which is defined for any state by

$$L_e \equiv N(e^-) - N(e^+) + N(\nu_e) - N(\bar{\nu_e}), \tag{2.2}$$

where $N(e^-)$ is the number of electrons present, and so on. For single-particle states, $L_e = 1$ for e^- and ν_e, $L_e = -1$ for e^+ and $\bar{\nu_e}$, and $L_e = 0$ for all other particles.

The form of Equation 2.2 also applies to the heavier lepton generations. Finally, in the SM, lepton numbers are individually conserved in all known interactions.

2.2.1.2 Quarks

Currently, there are six known quarks in the SM. Like the leptons, these six distinct types, or flavors, occur in pairs, or generations, denoted

$$\begin{pmatrix} u \\ d \end{pmatrix}, \begin{pmatrix} c \\ s \end{pmatrix}, \begin{pmatrix} t \\ b. \end{pmatrix} \tag{2.3}$$

Each generation consists of a quark with electromagnetic charge +2/3 (u,c, or t) together with a quark of charge -1/3 (d,s,b), in units of q. They are called the down(d), up(u), strange(s), charmed(c), bottom(b) and top(t) quarks. Each of these particles has an anti-particle version, with the same quantum numbers, but opposite charge. Furthermore, each quark also carries a *color charge* which can be red, green, or blue. This is a result of the strong force interaction of the quarks and will be explained in more detail in Section 2.3.3.

Quarks are known to bound to other quarks in states that we call hadrons. Hadrons can be bound states of two or three quarks called mesons and baryons, respectively. Recently, the LHCb collaboration reported the observation of a new type of hadron, a so-called *pentaquark*, which is a bound state composed of four quarks and one anti-quark[15].

2.2.2 Bosons

The SM bosons are the mediators of the interaction between the matter content of the SM, but also within themselves. They have integer spin quantum numbers and follow Bose-Einstein statistics, which means that they are not limited to single occupancy of the same quantum state.

There are 6 named bosons: the gluon, the photon, the $W^{\pm}$, and the Z, which have spin 1; and the Higgs boson, which corresponds to a scalar field and therefore has spin 0.

2.3 Particle Interactions

The interactions of the particles described in the previous section can be described in the mathematical framework of gauge field theory. Three of the four fundamental forces of nature are described in the SM (electromagnetism, the strong and the weak force). To each of these forces belongs a physical theory, its corresponding charge, (i.e. electric charge, color or flavor) and an associated boson as mediator.

Charges correspond to the time-invariant generators of a symmetry group, and specifically, to the generators that commute with the Hamiltonian. The invariance of the charge corresponds to the vanishing commutator

$$[Q, H] = 0 \tag{2.4}$$

for a given charge Q and Hamiltonian H. Thus charges are associated with conserved quantum numbers; which are the eigenvalues q of the generator Q [16].

Modern theories describe these forces in terms of quantum fields, namely quantum electrodynamics (QED), QCD and the unified electroweak quantum field theory. One feature all these theories have in common is that they are all gauge invariant. This is important because it is a fundamental requirement from which the detailed properties of the interaction are deduced, as we shall see later in this section.

To describe each of the three SM interactions or forces, we will start with a Lagrangian that describes the general dynamics of a given system of particles. Then we will study its invariance(variance) under a global(local) gauge transformation. We will see that in order to maintain gauge invariance after a local transformation, we will need to introduce additional gauge fields and their corresponding covariant derivatives. Finally, we will take a look at the conservation laws arising from the symmetry of the gauge invariance [17].

2.3.1 Quantum Electrodynamics

QED describes the dynamics of the electromagnetic interaction between fermions and the boson mediating the interaction, the photon. QED corresponds to the U_{EM} group and it was the first discovered example of gauge symmetry.

In QFT, particles are represented by fields[18], which are in turn represented mathematically by Lagrangian densities $\mathcal{L}$. If we start with the Lagrangian density for the Dirac spin-1/2 fermion field[19]

$$\mathcal{L} = \bar{\psi}(i\gamma^{\mu}\partial_{\mu} - m)\psi \tag{2.5}$$

where γ^{μ} are the gamma matrices[20], ψ is a four-component column vector representing the wave function of a spin 1/2 particle (or Dirac spinor), $\bar{\psi} = \psi^{\dagger}\gamma^{0}$, and m is the mass of the particle. The Lagrangian is invariant under a global U(1) transformation of the form

$$\psi \rightarrow \psi' = e^{-i\alpha}\psi \tag{2.6}$$

while the parameter α is kept a constant. If instead, α is allowed to vary as a function of space-time, then Equation 2.6 becomes a local U(1) transformation and the Lagrangian density becomes

$$\mathcal{L} \rightarrow \mathcal{L}' = \mathcal{L} + \bar{\psi}\gamma^{\mu}(\partial_{\mu}\alpha(x))\psi \tag{2.7}$$

which is not invariant under the local transformation.

In order to restore local gauge invariance, a gauge field A_{μ} representing the photon and the covariant derivative

$$D_{\mu} = \partial_{\mu} + iqA_{\mu} \tag{2.8}$$

, where q (electric charge) are introduced. The new gauge field transforms as

$$A_\mu \rightarrow A'_\mu = A_\mu + \partial_\mu \chi(x) \tag{2.9}$$

, where $\chi(x)$ is an arbitrary function of space-time. The covariant derivative has the same transformation properties as ψ and is chosen to replace ∂_μ.

After introducing these modifications, the Lagrangian takes the form:

$$\mathcal{L} = \bar{\psi}(i\gamma^\mu D_\mu - m)\psi - \frac{1}{4} F_{\mu\nu} F^{\mu\nu} \tag{2.10}$$

where $F_{\mu\nu} = \partial_\mu A_\nu - \partial_\nu A_\mu$ is the electromagnetic field strength tensor.

By looking at the resulting Lagrangian after the introduction of new gauge fields we can see that it does not include a mass term for the photon field (i.e. no term proportional to $m^2 A_\mu A^\mu$). At this point, the theory posits an infinite range for the interaction (which is experimentally verified).

The final form of the Lagrangian includes lepton-photon interactions, as well as those in the form of $l^+ l^- \gamma$ and a quadratic term in the field strength tensor which is the photon kinetic energy. It can be generalized to include all the electromagnetically-charged fermions in the SM by taking the form

$$\mathcal{L} = \sum_i \bar{\psi}_i(i\gamma^\mu D_\mu - m_i)\psi_i - \frac{1}{4} F_{\mu\nu} F^{\mu\nu} \tag{2.11}$$

where $i = e, \mu, \tau, u, d, c, s, t, b$.

2.3.2 Electroweak Interaction

The story of weak interactions starts with Henri Becquerel's discovery of radioactivity in 1896 and its subsequent classification into alpha, beta and gamma decays of the nucleus by Ernest Rutherford and others. But the real understanding of beta-decay in the sense we now know it came only after Enrico Fermi formulated a physical mechanism for such process in 1934.

The main ingredient for Fermi's theory had been provided by Wolfgang Pauli. To solve the puzzle of the continuous energy spectrum of the electrons emitted in the beta-decay of the nuclei, Pauli had suggested that along with the electron, an almost massless neutral particle was also emitted. Fermi succeeded in incorporating Pauli's suggestion and thus was born the theory of weak interactions [21].

In the 1960s Glashow, Salam, and Weinberg had developed a theory[22, 23, 24] that unified electromagnetic and weak interactions in a way that is often compared to the unification of electric and magnetic interactions by Faraday and Maxwell a century earlier. This new theory made several remarkable predictions, including the existence of a neutral vector boson Z^0 and of weak reactions arising from its exchange.

The EW interaction is based on a local $SU(2)_L \times U(1)_Y$ gauge symmetry where L and Y are the generators of the symmetry. Here, electromagnetic and weak interactions are unified into a single non-abelian gauge theory. In order to understand this unification, we will start with a fermionic doublet representing an $SU(2)$ symmetry

$$\psi = \begin{pmatrix} \psi_1(x) \\ \psi_2(x) \end{pmatrix}, u_R, d_R \tag{2.12}$$

which transforms under the three dimensional rotation

$$\psi \to exp < i\alpha^i \frac{\sigma_i}{2} > \psi \tag{2.13}$$

which is the three dimensional version of Equation 2.6 and σ^i are the Pauli sigma matrices: the three non-commuting generators of the SU(2) transformations.

Just like in Section 2.3.1, we allow the parameter α to vary as a function of space-time so that

$$\psi(x) \to V(x)\psi(x) \tag{2.14}$$

, where $V(x) = exp(i\alpha^i(x)\frac{\sigma^i}{2})$.

In order to keep the Lagrangian invariant under this transformation, we introduce additional fields. Since SU(2) has three generators there are also three gauge fields $A^i_\mu(x)$. The covariant derivative for a SU(2) gauge invariant Lagrangian is

$$D_\mu = \partial_\mu - igA^i_\mu \frac{\sigma^i}{2} \tag{2.15}$$

and therefore

$$A^i_\mu(x)\frac{\sigma^i}{2} \rightarrow V(x)(A^i_\mu(x)\frac{\sigma^i}{2} + \frac{i}{g}\partial_\mu)V^\dagger(x) \tag{2.16}$$

To simplify this calculation, we can expand $V(x)$ to first order in α

$$A^i_\mu \frac{\sigma^i}{2} \rightarrow A^i_\mu \frac{\sigma^i}{2} + \frac{1}{g}(\partial_\mu \alpha^i)\frac{\sigma^i}{2} + i[\alpha^i \frac{\sigma^i}{2}, A^i_\mu \frac{\sigma^i}{2}] + ... \tag{2.17}$$

The covariant derivative will have the form

$$D_\mu \psi \rightarrow (1 + i\alpha^i \frac{\sigma^i}{2})D_\mu \psi \tag{2.18}$$

Due to the non-commutativity of the generators of this symmetry, the field strength tensor has an extra term

$$F^i_{\mu\nu} = \partial_\mu A^i_\nu - \partial_\nu A^i_\mu + g\epsilon^{ijk}A^j_\mu A^k_\nu \tag{2.19}$$

We can the construct the Yang-Mills Lagrangian

$$\mathcal{L} = -\frac{1}{4}(F^i_{\mu\nu})^2 + \bar{\psi}(i\gamma^\mu \partial_\mu - igA^i_\mu \frac{\sigma^i}{2})\psi \tag{2.20}$$

Now we introduce the local gauge invariance requirement for the Lagrangian and introduce new gauge fields with their associated covariant derivatives.

But first, we should note that the SM fermions possess a fundamental property called chirality, which describes how a given particle's wave function behaves under rotation. In the SM, the left-handed components of the electron neutrino and electron are grouped into an SU(2) doublet. Since the right-handed component of the electron is invariant under SU(2), it is placed in a singlet, i.e.:

$$L_e = \begin{pmatrix} \nu_e \\ e_L \end{pmatrix}, e_R \tag{2.21}$$

And so on for the heavier generations of leptons.

Within the SM framework, neutrinos are weakly-interacting massless particles. As such, neutrinos wouldn't be able to change their handedness, but with mass, they can. Until now there is no experimental evidence for right handed neutrinos.

The kinetic energy term of the electroweak Lagrangian for first generation leptons can be represented by:

$$\mathcal{L}^e_{KE} = L_e^\dagger \tilde{\sigma}^\mu i\partial_\mu L_e + e_R^\dagger \sigma^\mu i\partial_\mu e_R \tag{2.22}$$

where $\sigma = (\sigma^0, \sigma^1, \sigma^2, \sigma^3)$, $\tilde{\sigma} = (\sigma^0, -\sigma^1, -\sigma^2, -\sigma^3)$, σ^0 is an identity matrix, and the σ^i are again the Pauli matrices. This Lagrangian is invariant under the global $SU(2)_L \times U(1)_Y$ transformation:

$$L \rightarrow L' = e^{i\theta} UL \tag{2.23}$$

$$e_R \rightarrow e'_R = e^{2i\theta} e_R \tag{2.24}$$

where

$$U = e^{-ia^k \sigma^k} \tag{2.25}$$

and θ and a^k are real numbers parameterizing the transformation.

Again, the Lagrangian is not invariant under a transformation where these parameters are allowed to vary as a function of space-time, i.e. a local transformation.

To restore invariance, we can introduce additional gauge fields and replace the space-time derivatives with an appropriately chosen covariant derivative. This time, we introduce a U(1) gauge field $B_\mu(x)$ and three SU(2) gauge fields $W_\mu(x) = W_\mu^k(x)\sigma_k$. Such fields must transform as

$$B_\mu(x) \to B'_\mu(x) = B_\mu(x) + \frac{2}{g_1}\partial_\mu\theta(x) \tag{2.26}$$

$$W_\mu(x) \to W'_\mu(x) = U(x)W_\mu(x)U^\dagger(x) + \frac{2i}{g_2}(\partial_\mu U(x))U^\dagger(x) \tag{2.27}$$

where g_1 and g_2 are dimensionless parameters of the theory, the coupling strengths of the interactions. The necessary covariant derivatives are given by

$$D_\mu L_e = (\partial_\mu + i\frac{g_1}{2}YB_\mu + i\frac{g_2}{2}W_\mu)L_e \tag{2.28}$$

$$D_\mu e_R = (\partial_\mu + i\frac{g_1}{2}YB_\mu)e_R \tag{2.29}$$

where Y is the weak hypercharge operator, whose eigenvalues are listed in Table 2.1. The weak hypercharge values can be calculated as $Y = 2(Q - T_3)$, where T_3 is the third component of the weak isospin quantum number T.

	Particle	Q	T_3	Y	B	L
Quarks	$q_L = \begin{pmatrix} u \\ d \end{pmatrix}_L$	$\begin{pmatrix} 2/3 \\ -1/3 \end{pmatrix}$	$\begin{pmatrix} 1/2 \\ -1/2 \end{pmatrix}$	1/3	1/3	0
	u_R	2/3	0	4/3	1/3	0
	d_R	-1/3	0	-2/3	1/3	0
Leptons	$l_L = \begin{pmatrix} \nu_e \\ e \end{pmatrix}_L$	$\begin{pmatrix} 0 \\ -1 \end{pmatrix}$	$\begin{pmatrix} 1/2 \\ -1/2 \end{pmatrix}$	-1	0	1
	e_R	-1	0	-2	0	1

Table 2.1: Quantum numbers of the SM fermions

The covariant derivatives transform according to the same rule as the fields themselves. Combining the kinetic and gauge interaction terms of the Lagrangian yields

$$\mathcal{L} = \mathcal{L}_{KE} + \mathcal{L}_{gauge} = L_e^\dagger \tilde{\sigma}^\mu i D_\mu L_e + e_R^\dagger \sigma^\mu i D_\mu e_R - \frac{1}{4} B_{\mu\nu} B^{\mu\nu} - \sum_{i=1}^{3} \frac{1}{4} W^i_{\mu\nu} W^{i\mu\nu} \tag{2.30}$$

where $B_{\mu\nu} = \partial_\mu B_\nu - \partial_\nu B_\mu$ and $W_{\mu\nu} = [\partial_\mu + (\frac{ig_2}{2})W_\mu]W_\nu - [\partial_\nu + (\frac{ig_2}{2})W_\nu]W_\mu$ are the field strength tensors. This Lagrangian is now locally invariant.

The mediators of the electroweak force are the physical bosons $W^\pm$, the Z and the photon. All of them result from the combination of the newly introduced gauge fields as in the following way

- The $W^\pm$ are linear combinations of the W_1 and W_2, which are electrically charged and given by

$$W^\pm_\mu = \frac{W^1_\mu \mp iW^2_\mu}{\sqrt{2}} \tag{2.31}$$

- The W_3 and B gauge fields are electrically neutral. The physical Z and photon are linear combinations of these fields, given by

$$Z_\mu = W^3_\mu cos\theta_W - B_\mu sin\theta_W \tag{2.32}$$

$$A_\mu = W^3_\mu sin\theta_W - B_\mu cos\theta_W \tag{2.33}$$

  where the Weinberg angle θ_W is defined by $sin\theta_W = g_1/\sqrt{g_1^2 + g_2^2}$.

The interactions contained in the Lagrangian couple the $W^\pm$ bosons to the left-handed lepton components only, unlike the photon and Z bosons which couple to both the left- and right-handed components.

Furthermore, we can now assign a value to the electromagnetic charge e proportional to the interaction strength

$$g_2 sin\theta_W = g_1 cos\theta_W = e. \tag{2.34}$$

Finally, in order to include second and third generation leptons, the leptonic portion of the Lagrangian generalizes to

$$\mathcal{L}^l = \sum_{leptons} (L_e^\dagger \tilde{\sigma}^\mu i D_\mu L_e + e_R^\dagger \sigma^\mu i D_\mu e_R) - \frac{1}{4} B_{\mu\nu} B^{\mu\nu} - \sigma_{i=1}^3 \frac{1}{4} W_{\mu\nu}^i W^{i\mu\nu} \tag{2.35}$$

Quarks are included in the EW sector in a similar manner. The left-handed components of the u and d quark are placed in SU(2) doublets, and the right-handed components in singlets.

$$Q_u = \begin{pmatrix} u_L \\ d_L \end{pmatrix}, u_R, d_R \tag{2.36}$$

The second and third generation quarks can be represented in the same way. The covariant derivatives acting on the quark fields have the same form as those which act on the lepton fields. Therefore, the dynamic portion of the u and d quark Lagrangian is given by

$$\mathcal{L}_{KE}^q = \sum_{quarks} Q_u^\dagger \tilde{\sigma}^\mu i D_\mu Q_\mu + u_R^\dagger \sigma^\mu i D_\mu u_R + d_R^\dagger \sigma^\mu i D_\mu d_R \tag{2.37}$$

Again, the W bosons couple only to the left-handed quark components, while the Z and photon couple to the right-handed components as well.

The full electroweak Lagrangian is a result of the addition of the lepton and quark kinetic components, as well as the gauge interaction component.

$$\mathcal{L}^{EW} = \mathcal{L}_{KE}^l + \mathcal{L}_{KE}^q + \mathcal{L}_{gauge} \tag{2.38}$$

Note that a U(1) transformation of the form $L_{e,\mu,\tau} \rightarrow e^{i\alpha} L_{e,\mu,\tau}$, $e, \mu, \tau_R \rightarrow e, \mu, \tau^{i\alpha} e, \mu, \tau_R$ leaves the EW Lagrangian invariant, which leads to conservation of lepton number. Additionally, a U(1) transformation multiplying all negatively (positively) charged fields by $e^{i\alpha}(e^{-i\alpha})$ leaves the Lagrangian invariant, and implies conservation of electric charge.

On the other hand, the EW Lagrangian is not invariant under charge conjugation C or a parity transformation P. Charge conjugation is the operation of exchanging all particles with antiparticles and vice-versa. A parity transformation is the inversion of spatial coordinates, $r \to -r$. The neutral current interactions, mediated by the Z and photon, preserve combined CP invariance. However, combined CP symmetry is violated by weak current interactions, mediated by the $W^{\pm}$, in the quark sector. A third important potential symmetry is time reversal T, where $t \to -t$. Combined CPT invariance is required to maintain Lorentz invariance. Therefore, the breaking of CP also implied the breaking of T symmetry.

Although CP is not conserved, there is good reason to believe that all interactions are invariant under the combined operation of CPT, taken in any order. This result is called the CPT theorem[25] and can be shown to hold in any relativistic quantum theory in which signals cannot propagate faster than the speed of light.

2.3.3 Strong Interaction

QCD is the theory that describes the interaction between quarks via the strong force. It is represented by a local $SU(3)_C$ gauge symmetry and the interaction mediator is the gluon.

Associated with the $SU(3)_C$ symmetry are several conserved quantum numbers, called color charges, which play a similar role in strong interactions to that played by e in electromagnetic interactions. Color charges can be green, red, and blue but only color neutral (or colorless) states have been observed in nature. Baryons contain equal parts of each color and mesons contain color-anticolor pairs.

In QCD, quarks are represented in this theory as color triplets

$$q_u = \begin{pmatrix} u_r \\ u_g \\ u_b \end{pmatrix} \tag{2.39}$$

and gluons contain two color charges. The eight known combinations of color charges for the gluon are represented by eight gauge fields that are a direct consequence of the 8 non-abelian generators of SU(3), the Gell-Mann matrices[26].

As in the previous sections, we start building the interaction from an $SU(3)$ Lagrangian that is globally invariant in the form

$$\mathcal{L}^q_{QCD} = \sum_{i=1}^{6} \bar{q}_i i\gamma^\mu \partial_\mu q_i \tag{2.40}$$

This Lagrangian is invariant under a transformation of the form $q_i \to q_i' = Uq_i$ where U is a member is a member of $SU(3)$. If we allow for a transformation of the form $U(x)$, the Lagrangian is no longer invariant. To return invariance, we introduce 8 gauge fields ($G_\mu(x)$) which represent the gluon fields and an appropriate covariant derivative. They will transform as

$$G_\mu \to G_\mu' = UG_\mu U^\dagger + \frac{i}{g_s}(\partial_\mu U)U^\dagger \tag{2.41}$$

$$D_\mu q_i = (\partial_\mu + ig_s G_\mu)q_i \tag{2.42}$$

where g_s is the dimensionless coupling strength of the color interaction.

The field strength tensor for QCD is:

$$G_{\mu\nu} = \partial_\mu G_\nu - \partial_v G_\mu + ig_s(G_\mu G_\nu - G_\nu G_\mu) \tag{2.43}$$

and the locally $SU(3)$ gauge invariant QCD Lagrangian is then given as:

$$\mathcal{L}^q_{QCD} = \sum_{i=1}^{6} (\bar{q}_i i\gamma^\mu D_\mu q_i) - \frac{1}{4}\sum_{i=1}^{8} G^i_{\mu\nu} G^{i\mu\nu} \tag{2.44}$$

In contrast to the EW interaction, C,P, and T are all conserved. The range of the strong force interaction is about 10^{-15} m, which is enough to act on nucleons, i.e. protons and neutrons to form atomic nuclei.

Finally, QCD is a strongly coupled theory at low energies and large distance scales, but weakly interacting at high energies and small distance scales. This fact is responsible for the hadronic bound states of quarks. Moreover, unlike QED, its mediator, the gluon, interacts with itself. At low energy scales, i.e. the non-perturbative regime, QCD calculations are extremely difficult and techniques as lattice gauge theory must be exploited. On the other hand, at a high energy scale, or equivalently small distance scales, the strong interaction becomes weakly interacting and quarks are effectively free. In this regime the usual techniques of perturbation theory can be used, allowing high-precision calculations.

2.3.4 Brout-Englert-Higgs Mechanism and the Higgs Boson

As we have seen from the previous section, the EW and QCD Lagrangians do not contain any mass terms. Gauge invariance seems to imply that the spin-1 gauge bosons have zero masses. This is acceptable for QED and QCD, where the gauge bosons are the photons and the gluons, which do indeed have zero mass. However, the $W\pm$ and Z^0 bosons are very heavy, and therefore, not massless as they would if gauge invariance was exact.

This problem is overcome by introducing the Brout-Englert-Higgs(BEH) mechanism which postulates that the various particles in the SM interact with a new type of scalar field, the Higgs field(s). This field differs from others in its behavior in the so-called vacuum state by having a non-zero value, unlike the other fields introduced previously. The value v is not invariant under a gauge transformation, and will spontaneously break the symmetry of the Lagrangian in a process we will refer to as spontaneous electroweak symmetry breaking (EWSB).

The Goldstone theorem postulates that for every spontaneously broken continuous symmetry there will be a new massive scalar "Goldstone" boson. The number of new bosons will be equal to the number of broken generators of the symmetry group. The massless SM bosons then acquire mas by absorbing these Goldstone bosons.

The BEH mechanism is also used to generate mass for the quarks and electrically charged leptons. The neutrinos, photon, and gluons remain massless, as observed experimentally.

Remember from previous section that there are four massless electroweak gauge bosons, W^1, W^2, W^3, and B^0. The experimentally observed bosons, however, are the massless photon, and three massive bosons (the $W^{\pm}$ and Z). We also know that electric charge Q is conserved in EW interactions. This means that the $SU(2)_L \times U(1)_Y$ EW theory is broken such that a new $U(1)_{EM}$ symmetry group is formed which corresponds to electromagnetism.

In order for three gauge bosons to acquire mass they must absorb three Goldstone bosons. The simplest method to accomplish this is to introduce a complex, scalar $SU(2)$ doublet Φ with hypercharge $Y = 1$.

$$\Phi = \begin{pmatrix} \Phi_A \\ \Phi_B \end{pmatrix} = \begin{pmatrix} \phi_1 \\ i\phi_2 \\ \phi_3 \\ i\phi_4 \end{pmatrix}, \tag{2.45}$$

The part of the SM Lagrangian which includes the EW gauge bosons and the leptons can be written as

$$\mathcal{L}_{SM} = -\frac{1}{4} W^a_{\mu\nu} W^{\mu\nu}_a - \frac{1}{4} B_{\mu\nu} B^{\mu\nu} + \bar{L}_i (iD_\mu \gamma^\mu) L_i + \bar{e}_{R,i} (iD_\mu \gamma^\mu) e_{R,i} \tag{2.46}$$

where i runs over the three generations, μ and ν are Lorentz indices, and a runs over the generators in the gauge group. The field strengths are given by

$$W^a_{\mu\nu} = \partial_\mu W^a_\nu - \partial_\nu W^a_\mu + g_2 \epsilon^{abc} W^b_\mu W^c_\nu \tag{2.47}$$

$$B_{\mu\nu} = \partial_\mu B_\nu - \partial_\nu B_\mu \tag{2.48}$$

and the covariant derivatives for the left- and right-handed leptons are

$$D_\mu L_L = (\partial_\mu - ig_2 T_a W^a_\mu - ig_1 Y B_\mu) L_L \tag{2.49}$$

$$D_\mu e_R = (\partial_\mu - ig_1 Y B_\mu) e_R \tag{2.50}$$

where T_a are the generators of the $SU(2)_L$ gauge group and g_1, g_2 are the coupling constants for the EW interaction.

The scalar part of the Lagrangian required by the addition of a scalar field is then

$$\mathcal{L}_S = (D_\mu \Phi)^\dagger (D^\mu \Phi) - V(\Phi^\dagger \Phi) \tag{2.51}$$

where the first term is the kinetic term and the second term is the scalar potential. While the form of the scalar potential is not known from first principles, we can make the assumption that it takes the form

$$V(\Phi^\dagger\Phi) = \mu^2\Phi^\dagger\Phi + \lambda(\Phi^\dagger\Phi)^2 \tag{2.52}$$

The value of λ must be positive in order for the vacuum to be stable. The sign of μ^2 specifies one of two cases for the potential.

- When $\mu^2 > 0$, the potential $V(\Phi)$ is always positive and has a minimum at

$$< 0|\Phi|0 >\equiv \Phi_0 = \begin{pmatrix} 0 \\ 0 \end{pmatrix} \tag{2.53}$$

  where no spontaneous symmetry breaking can occur.

- When $\mu^2 < 0$ the potential has a minimum value not located at the origin. In this case, the neutral component of the scalar field will acquire a vacuum expectation value v

$$< 0|\Phi|0 >= \Phi_0 = \frac{1}{\sqrt{2}}\begin{pmatrix} 0 \\ v \end{pmatrix} \tag{2.54}$$

  where $v = \sqrt{\frac{-\mu^2}{\lambda}}$

By only adding a vev to the neutral component of the scalar field, electromagnetism is unbroken and the $U(1)_{EM}$ symmetry keeps a conserved electric charge $Q = T_3 + \frac{Y}{2}$.

We can then expand the scalar field Φ around the minimum Φ_0 to get

$$\Phi(x) = \frac{1}{\sqrt{2}}\begin{pmatrix} 0 \\ v + h(x) \end{pmatrix} \tag{2.55}$$

where $h(x)$ is a new scalar field.

Next we insert this field into the kinetic part of the Lagrangian and redefine the gauge fields as

$$W_\mu^\pm = \frac{1}{\sqrt{2}}(W_\mu^1 \mp iW_\mu^2) \tag{2.56}$$

$$Z_\mu = \frac{1}{\sqrt{g_1^2 + g_2^2}}(g_2 W_\mu^3 - g_1 B_\mu) \tag{2.57}$$

$$A_\mu = \frac{1}{\sqrt{g_1^2 + g_2^2}}(g_2 W_\mu^3 + g_1 B_\mu) \tag{2.58}$$

which correspond to the observed gauge bosons.

After this the covariant derivative becomes

$$|D_\mu \Phi|^2 = \frac{1}{2}(\partial_\mu H)^2 + \frac{1}{2}g_2^2(v+H)^2 W_\mu^+ W^{\mu-} + \frac{1}{8}(v+H)^2(g_1^2+g_2^2)Z_\mu Z^\mu \tag{2.59}$$

From here we can see that the photon A_μ remains massless, but that the mass terms for the W and Z bosons take the general forms $M_W^2 W_\mu W^\mu$ and $M_Z^2 Z_\mu Z^\mu/2$ respectively.

Thus the masses of the electroweak gauge bosons are

$$M_W = \frac{1}{2} v g_2 \tag{2.60}$$

$$M_Z = \frac{1}{2} v \sqrt{g_1^2 + g_2^2} \tag{2.61}$$

$$M_A = 0 \tag{2.62}$$

Three of the degrees of freedom from the scalar field, which would have been two charged and one neutral Goldstone boson, have been absorbed by the gauge bosons in order to give them mass. There is one remaining degree of freedom, an oscillation in the radial direction of the scalar potential, which corresponds to the neutral Higgs boson.

Finally, fermions acquire mass by adding couplings between the fermion fields and the scalar field to the SM Lagrangian. The part of the Lagrangian that corresponds to the first generation fermions is given by

$$\mathcal{L}_F = -G_e \bar{L} \Phi e_R - G_d \bar{Q} \Phi d_R - G_u \bar{Q} \tilde{\Phi} u_R + h.c. \tag{2.63}$$

where $\tilde{\Phi} = i\tau_2 \Phi^*$ is the conjugate of Φ with negative hypercharge.

There are additional terms added to the full Lagrangian which correspond to the second and third generations which are not shown here.

By substituting Φ into the previous Lagrangian we find

$$\mathcal{L}_F = -\frac{1}{\sqrt{2}}[G_e \begin{pmatrix} \bar{\nu} & \bar{e} \end{pmatrix}_L \begin{pmatrix} 0 \\ v+H \end{pmatrix} e_R + G_d \begin{pmatrix} \bar{u} & \bar{d} \end{pmatrix}_L \begin{pmatrix} 0 \\ v+H \end{pmatrix} d_R + G_u \begin{pmatrix} \bar{u} & \bar{d} \end{pmatrix}_L \begin{pmatrix} 0 \\ v+H \end{pmatrix} u_R] + h.c. \tag{2.64}$$

$$= -\frac{1}{\sqrt{2}}(v+H)(G_e \bar{e}_L e_R + G_d \bar{d}_L d_R + G_u \bar{u}_L u_R) + h.c. \tag{2.65}$$

where $h.c.$ is a placeholder for the hermitian conjugate terms.

The fermion masses take the form $m\bar{f}_L f_R + h.c.$, which means that the fermion masses for the first generation are

$$m_e = \frac{G_e v}{\sqrt{2}}, m_u = \frac{G_u v}{\sqrt{2}}, m_d = \frac{G_d v}{\sqrt{2}} \tag{2.66}$$

The second and third generations have similar mass terms. For the case of the neutrinos, since there is no right handed neutrino in the SM the neutrinos that do exist remain massless.

Finally, the coupling constants, G, and the fermion masses are not predicted by the SM, so they must be measured and added to the model.

2.4 Beyond the Standard Model

The SM evolved in response to a series of experimental discoveries over a period of several decades, and it turned out to be a remarkably successful theory. At the present time, provided non-zero neutrino masses are incorporated, all experimental observations in particle physics are consistent with the SM, but there is no reason to suppose that there will not be more surprises in the future, as higher energy regions are explored.

Also, there are a few experimental facts which suggest that the SM may not be a complete theory of nature. For example, there is strong evidence that the particles of the SM can only account for a small fraction of the matter in the Universe, and the observed predominance of matter over antimatter cannot be understood in the framework of the SM.

Moreover, there is still an incompatibility between general relativity (GR) (which can be thought of as the theory of gravitation) and the SM (the theory that describes the other three fundamental forces) because space-time is not quantized in GR.

Finally, the SM itself embodies many assumptions and more than twenty free parameters, giving rise to many questions like

- Can the number of parameters be reduced?
- Why are there three generations of quarks and leptons, rather than just the one that is required to describe "ordinary matter", i.e. the neutrons and protons?
- Are the quarks really point-like particles, or will they turn out to be composite when we are able to explore a higher energy regime?
- Why does the weak interaction violate CP invariance, but not the strong interaction?

Many theories have been proposed to try to answer these and other questions, and a few experimental programs have been set up to test them.

2.5 Lepton universality

All known experimental data are consistent with the assumption that the interactions of the electron and its neutrino are identical with those of the muon and its associated neutrino and the tau and its neutrino, provided the mass differences are taken into account. This fundamental assumption is called the universality of lepton interactions.

We will illustrate universality of this rule by looking at the leptonic decays [27]

$$\mu^+ \to e^+ + \nu_e + \bar{\nu}_\mu, \tag{2.67}$$

$$\mu^- \to e^- + \bar{\nu}_e + \nu_\mu, \tag{2.68}$$

$$\tau^- \to \mu^- + \bar{\nu}_\mu + \nu_\tau, and \tag{2.69}$$

$$\tau^- \to e^- + \bar{\nu}_e + \nu_\tau \tag{2.70}$$

of the muon and tau leptons at rest.

To simplify the calculation, we will work to lowest order only and we will use the zero-range approximation (a zero-range point interaction with strength equal to the Fermi constant $G_F = 1.66 \times 10^{-5} GeV^{-2}$), since the masses of the leptons are very small compared with the rest energy of the W bosons mediating the weak interaction.

We start by considering the muon decay whose rate has the form (in the zero-range approximation)

$$\Gamma(\mu^- \to e^- + \bar{\nu}_e + \nu_\mu) = K G_F^2 m_\mu^5 \tag{2.71}$$

since we are assuming the electron and neutrino masses are zero. Here, K is a dimensionless constant whose value will depend on the precise form of the interaction. If we assume this is the same for muon and tau leptons the same argument gives

$$\Gamma(\tau^- \to e^- + \bar{\nu}_e + \nu_\tau) = K G_F^2 m_\tau^5 \tag{2.72}$$

Likewise, $e - \mu$ universality gives

$$\Gamma(\tau^- \to e^- + \bar{\nu}_e + \nu_\tau) = \Gamma(\tau^- \to \mu^- + \bar{\nu}_\mu + \nu_\tau) \tag{2.73}$$

This explains why the experimental branching ratios for the two leptonic decay modes of the tau lepton are, to a good approximation, equal. A full calculation, taking into account final state masses, gives the ratio $\Gamma(\tau^- \to \mu^- + \bar{\nu}_\mu + \nu_\tau)/\Gamma(\tau^- \to e^- + \bar{\nu}_e + \nu_\tau) = 0.973$, whereas the experimental value is 0.976 ± 0.003.

It also gives a relation between the μ and τ lifetimes

$$\tau_l = \frac{1}{\Gamma_{tot}} = \frac{B(l^- \to e^- \bar{\nu}_e \nu_l)}{\Gamma(l^- \to e^- \bar{\nu}_e \nu_l)} \tag{2.74}$$

where l can be the μ or τ lepton and Γ_{tot} is the total decay rate and therefore

$$B(l^- \to e^- \bar{\nu}_e \nu_l) = \frac{\Gamma(l^- \to e^- \bar{\nu}_e \nu_l)}{\Gamma_{tot}} \tag{2.75}$$

is the branching ratio. Experimentally, $B = 1$ and 0.1783 ± 0.0004 for $l = \mu$ and τ[28]. Thus from 2.67and 2.71 we have

$$\frac{\tau_\tau}{\tau_\mu} = \frac{B(\tau^- \to e^- \bar{\nu}_e \nu_\tau)}{B(\mu^- \to e^- \bar{\nu}_e \nu_\mu)} (\frac{m_\nu}{m_\tau})^5 = (1.326 \pm 0.003) \times 10^{-7} \tag{2.76}$$

This agreement, involving lifetimes that differ by seven orders of magnitude, is impressive evidence of the universality of lepton interactions.

2.6 B-hadron anomalies

So far, no definite violation of lepton universality has been observed. However, the wealth of data on rare leptonic and semi-leptonic b hadron decays that have been accumulated at the LHC so far seem to challenge the rule.

In particular, current data on rare $b \to sll$ decays show an intriguing pattern of deviations from the SM predictions both for branching ratios [29], [30],[31],[32],[33] and angular distributions[34], [35], [36].

The latest global fits find that data consistently points with high significance to a non-standard effect that can be described by a four-fermion contact interaction[37]

$$C_9(\bar{s}\gamma^{\nu}P_L b)(\bar{\mu}\gamma_{\nu}\mu). \tag{2.77}$$

Nonetheless, the main obstacle towards conclusively establishing a beyond-SM effect is the inability to exclude large hadronic effects as the origin of the apparent discrepancies. In this respect, observables in $b \to sll$ transitions that are practically free of hadronic uncertainties are of particular interest. Among them are lepton flavor universality ratios such as the branching ratios $R_K = \frac{BR(B^+ \to K^+\mu^+\mu^-)}{BR(B^+ \to K^+e^+e^-)}$ and $R_{K^*} = \frac{BR(B^+ \to K^*\mu^+\mu^-)}{BR(B^+ \to K^*e^+e^-)}$.

In the SM, the only sources of lepton flavor universality violation are the leptonic Yukawa couplings, which are responsible for both the charged lepton masses and their interactions with the Higgs. However, Higgs interactions do not lead to any observable effects in rare b decays and lepton mass effects become relevant only for a very small dilepton invariant mass squared (q^2) close to the kinematic limit $q^2 \sim 4m_l^2$.

Over a broad range of q^2 the SM accurately predicts $R_k = R_{k^*} = 1$, with theoretical uncertainties on the order of 1%[38] which contradict experimental results which show a deviation from the expected SM value in the 2.4-2.6 σ range. A more recent study[39], [40] combined the results for R_K and R_{K^*}, resulting in a 4σ deviation from the SM.

2.6.1 $b \to s$ quark transitions

As we have seen from the previous section, over the last few years, many observables related to the flavour-changing neutral-current(FCNC) transitions $b \to l^+l^-$ have exhibited important deviations from SM expectations. Therefore, in this section, we will take a closer look at these

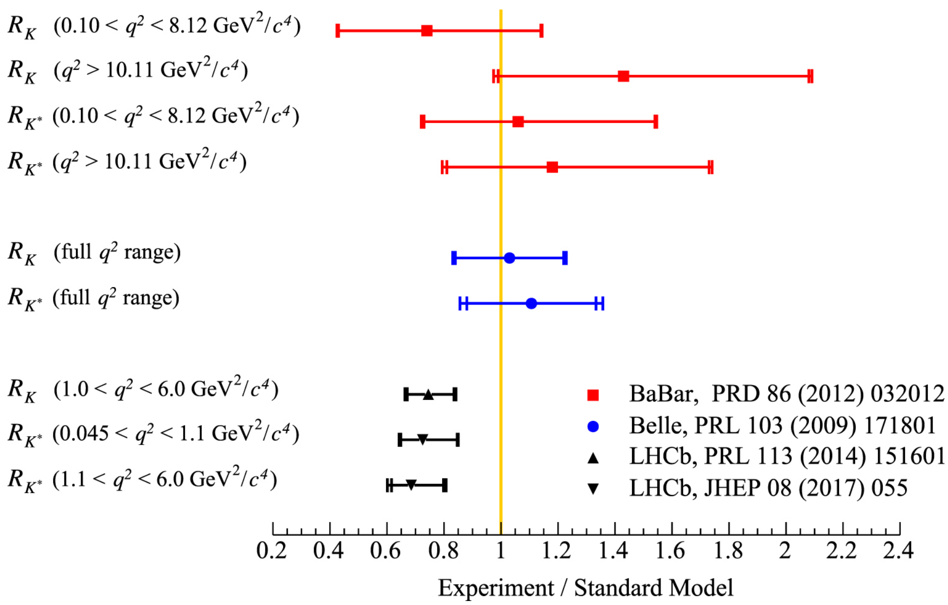

Figure 2.2: Summary of the $R_{K^{(*)}}$ measurements performed at the B-factories and by the LHCb experiment. Results are presented using different colored markers. The (yellow) vertical line corresponds to the SM prediction. Reprinted from [41]

transitions and their sensitivity to potential new physics.

A $b \to s$ quark transition is an example of a FCNC process[42]. In such process, the s and b quark interact via a quantum-loop transition involving predominantly a W boson and either and up, charm, or top quark as shown in Figure 2.3.

Within the SM, the lowest order processes that could mediate the $b \to s$ quark transitions are at least of third order and are suppressed by angular momentum conservation and by the chiral nature of the weak force. This suppression is not necessarily present for new-physics particles and that's what makes the study of this decay of particular interest in probing for physics beyond the SM.

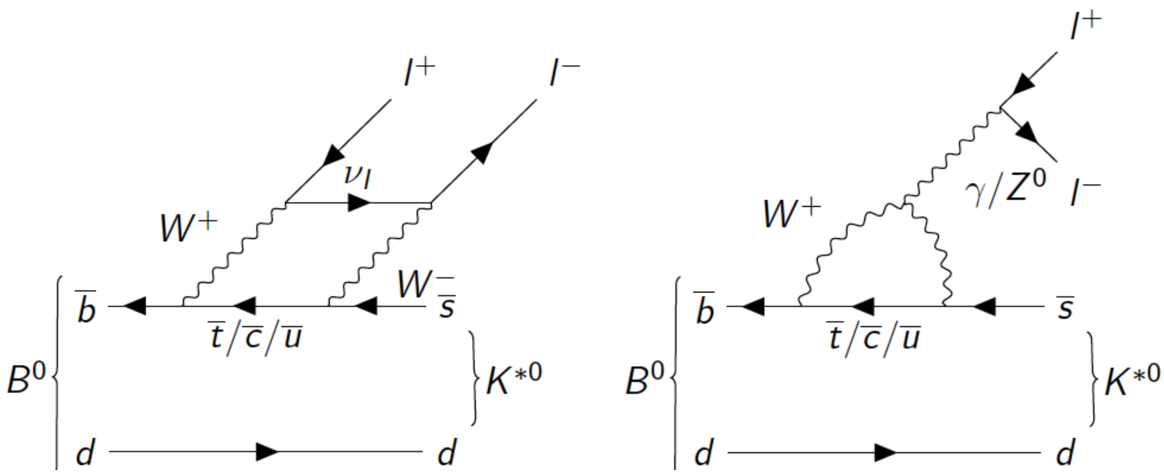

Figure 2.3: Lowest order Feynmann diagrams for $b \to s$ quark transition.

2.7 The Z'

There is a multitude of new-physics models that could explain some or all of the b decay anomalies. One example of an extension to the SM that could explain these deviations involves a heavy version of the Z boson, denoted Z'[43]. Such an extension to the model must satisfy direct searches for such particles at the CMS[44], [45] and ATLAS [46] experiments, which in practice means either that the Z' candidate must be at least 30 times heavier than the SM Z boson, or that it must have small couplings to the up and down quarks. If the Z' is very heavy, it would not have a sizable impact on the decay compared with the SM contribution, unless it could change the flavor of quarks directly without going through a quantum-loop transition.

A generic framework of a minimal extension to the SM which explains B anomalies has been introduced in [47] and we collect here only those formulae of that paper that are essential for our study. The new physics contribution to rare B decays can be described by the following effective Lagrangian

$$\mathcal{L} \supset \frac{4G_F}{\sqrt{2}} V_{tb} V_{ts}^* \frac{e^2}{16\Pi^2} C_9 O_9 + h.c. \tag{2.78}$$

where C_9 is a Wilson coefficient and the effective operator O_9,

$$O_9 = (\bar{s}\gamma_\mu P_L b)(\bar{\mu}\gamma^\mu \mu) \tag{2.79}$$

describes a four-fermion interaction, with a left-handed $b - s$ current and a vector current for μ. To fit the current data [48], the new physics contribution to C_9 needs to be $-1.59^{+0.46}_{-0.56}$.

In this model, an extra $U(1)$ gauge group has been introduced, resulting in a new gauge boson, the Z'. This newly introduced particle would have a flavor changing quark coupling δ_{bs} and a nonuniversal lepton coupling.

Including the contribution from Equation 2.78, the dominant terms in the Lagrangian that are allowed by all the existing constraints in order to address the anomalies are then

$$\mathcal{L} \supset Z'_\mu[g_\mu \bar{\mu}\gamma^\mu \mu + g_\mu \bar{\nu}_\mu \gamma^\mu P_L \nu_\mu + g_b \sum_{q=t,b} \bar{q}\gamma^\mu P_L q (g_b \delta_{bs} \bar{s}\gamma^\mu P_L b + h.c.)] \tag{2.80}$$

The Z' mass is constrained to be less than 5.5(10) TeV in the 1(2)σ range to explain the B anomalies[49]. As the mass gap between the Z' and the SM Z becomes smaller, interference problems start to arise and becomes harder to probe at the LHC. Therefore, for this analysis the lower bound in the search is 250 GeV.

2.7.1 4b Bottom Fermion Fusion

As we can conclude from Equation 2.80, the Z' does not significantly couple to first or second generation quarks, which could explain why it has not been observed experimentally yet. However, the Z' can be produced through its couplings to b quarks originating either from sea quarks, or gluon-splitting.

Therefore, the Z' is associated either with two,one, or no b-jets depending on the number of quarks from gluon splitting. The Z' can decay into pairs of b quarks, muons, muon neutrinos, and, if kinematically allowed, top quarks.

The relevant final states at the LHC are dimuon or di-b resonances. The cross sections behave as follows:

$$\sigma(pp \to Z' \to \mu\mu) \propto 2g_b^2(1 + k\delta_{bs}^2)g_\mu^2 \tag{2.81}$$

$$\sigma(pp \to Z' \to b\bar{b}) \propto 3g_b^4(1 + k\delta_{bs}^2) \tag{2.82}$$

where δ_{bs} regulates the possible production of Z' through b-s quark fusion, and where k contains the s-quark PDF contributions.

For this analysis, the special case when the Z' is associated with two b-jets coming from gluon splitting (a process we will refer to as Bottom Fermion fusion (BFF) (see Figure 2.4))and has a di-b jet final state is considered.

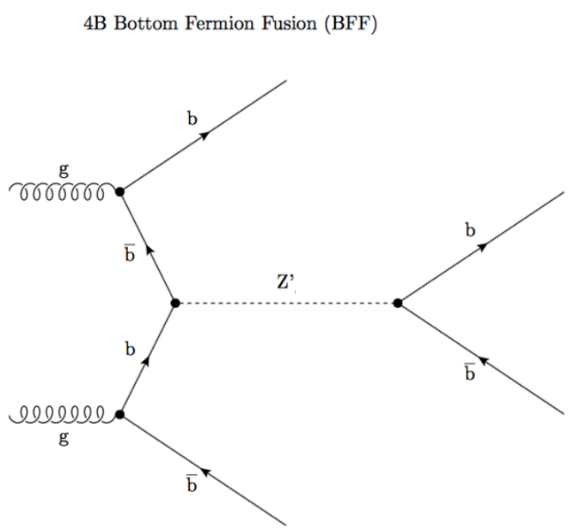

Figure 2.4: Feynman diagram for bottom fermion fusion (BFF).

2.7.2 Flavour-violating coupling δ_{bs}

In order to provide an explanation for B-decay anomalies, we need to consider the flavour-violating coupling δ_{bs}. Allowing the Z' boson to couple to s quarks in addition to b quarks results in two times more ways to produce the Z' and two times more ways for it to decay. A non-zero δ_{bs}

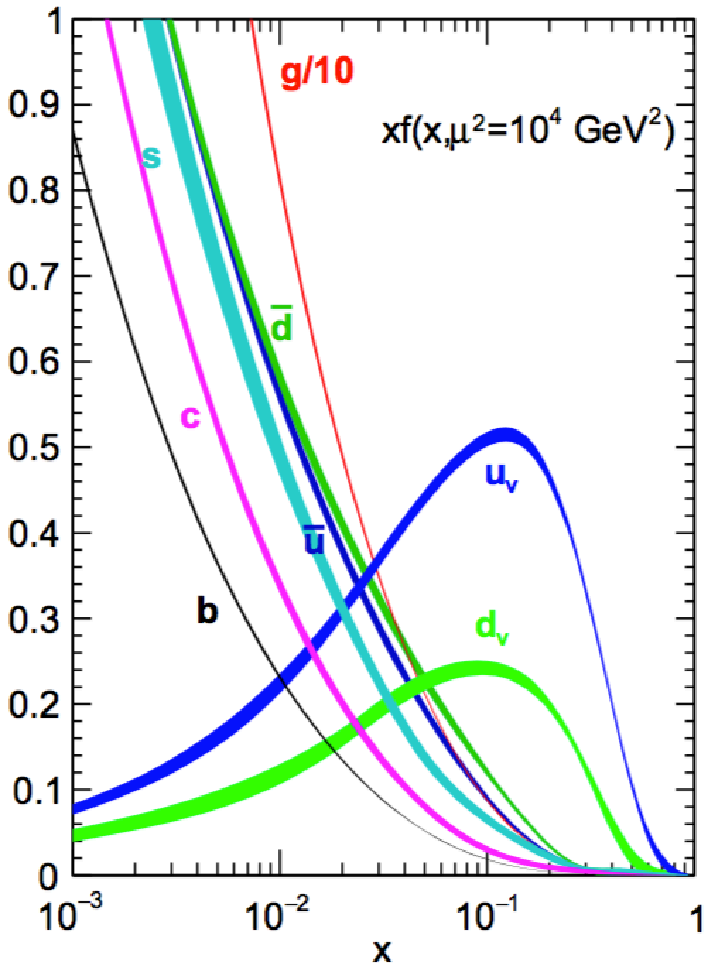

Figure 2.5: PDF for the LHC Run II. Reprinted from [2].

will allow the Z's to be produced by b and $\bar{s}$ quarks (in addition to $b\bar{b}$ ones) and this significantly enhances the production cross section since the PDF for the s quark is significantly higher than that for the b quark at the LHC, as we can see from Figure 2.5.

Also, we can see from Equation 2.82 and 2.81 that when δ_{bs} goes to zero, the flavor conserving contribution dominates the production of Z'. Likewise, when δ_{bs} is large but still satisfies the B anomalies (so smaller g_b) the flavour violating contribution dominates.

3. The LHC and CMS Detector

3.1 The Large Hadron Collider

The Large Hadron Collider (LHC) [50] experiment at the European Organization for Nuclear Research (CERN) is the world's largest and most powerful particle accelerator in operation today. Located at the border between Switzerland and France, it consists of a 27-km circumference ring of superconducting magnets and accelerating structures.

Within the ring, protons are accelerated to a speed close to that of light and made to collide at 4 points:

- CMS (Compact Muon Solenoid) [51],
- ATLAS (A Toroidal LHC ApparatuS) [52],
- ALICE (A Large Ion Collider Experiment) [53],
- and LHCb (Large Hadron Collider beauty) [54].

ATLAS and CMS are two general-purpose particle detectors located at opposite sides on the LHC ring. These are "onion-type" detectors in the sense that their general layout surrounds the interaction point with sub-detector systems aimed to measure a specific property of the particle to be detected.

The other two detectors, ALICE and LHCb are designed for specific purposes, like studying heavy-ion collisions and performing precision measurements of CP-violation and the physics of B-mesons, respectively. For this study, data collected by the CMS experiment is used.

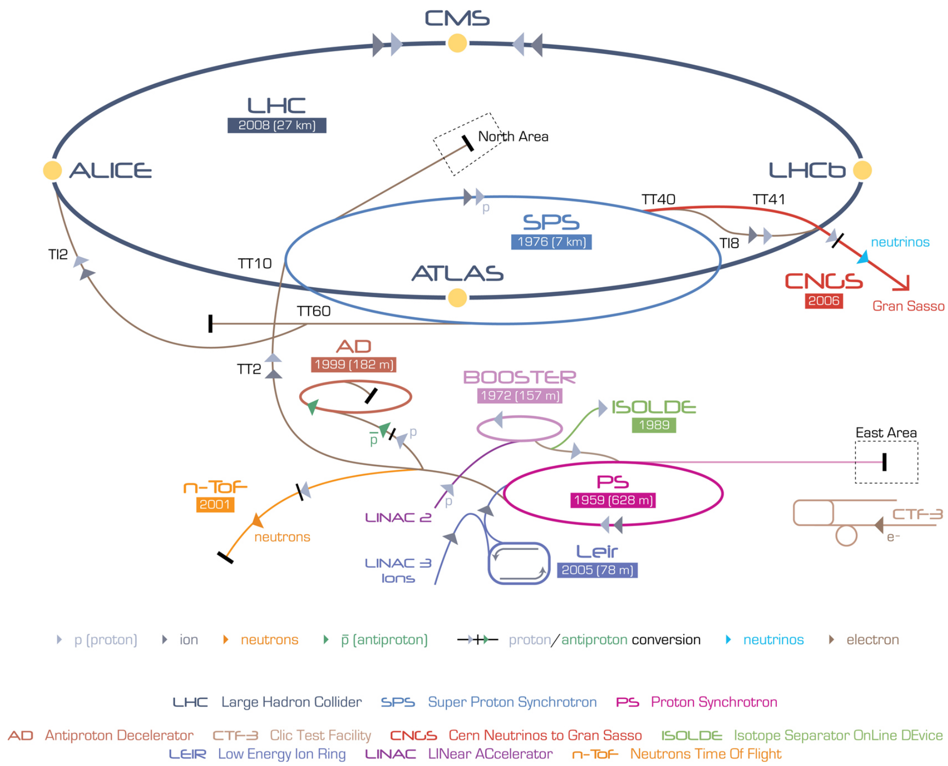

Figure 3.1: Schematic diagram for the LHC experiment at CERN. Retrieved from [3].

According to Einstein's famous equation $E = mc^2$, energy and mass are interchangeable. Therefore in order to produce heavy particles, a large amount of energy is required. The LHC was designed to produce highly energetic proton-proton, lead-proton or lead-lead beam collisions in which a variety of elementary particles can be produced.

The beams circulating the LHC ring are not continuous streams of particles, but rather trains of regularly spaced proton bunches. The experiment was designed to operate with 2,808 bunches of protons per beam, containing about 1.5×10^{11} protons per bunch separated by 25 ns, corresponding to a collision frequency of 40 MHz.

The LHC started operation in November 23, 2009. Through its 2010-2011 run, the LHC operated at a center-of-mass energy of 7 TeV. Then in 2012, the energy was increased to 8 TeV, and again to 13 TeV in 2015, after a shutdown in 2013 that lasted two years.

3.2 The CMS Detector

The CMS detectors was designed with the goal of identifying the particles coming out of the proton-proton collisions as well as to characterize their momentum, position, and trajectory at the moment of the collision. The goals of the CMS physics program range from studying the SM (including the Higgs boson) to searching for extra dimensions and dark matter. It even has a very successful heavy ion program.

In particular, the central feature of the CMS apparatus is a superconducting solenoid of 6 m internal diameter, providing a magnetic field of 3.8 T. The solenoidal volume contains a silicon pixel and strip tracker, a lead tungstate crystal electromagnetic calorimeter (EMCAL) and a brass and scintillator hadron calorimeter (HCAL). Each layer of the detector exploits a property of the particle to be detected to measure its energy, momentum, position, and direction.

The CMS detector was not built on site like other giant detectors of the LHC experiment, but it was constructed in 15 sections at ground level before being lowered into an underground cavern near Cessy in France and then reassembled. The complete detector is 21 m long, 12 m wide and 15 m high.

The layout of the detector can be seen in Figure 3.2. The following sections will describe each of the sub-detectors and its properties.

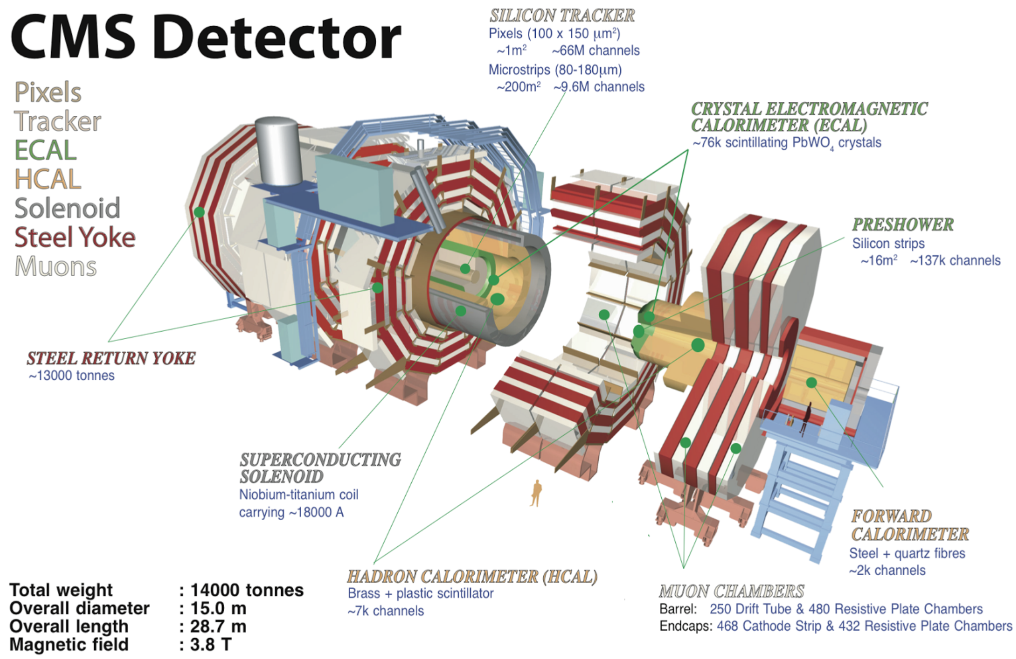

Figure 3.2: Schematic diagram for the CMS experiment with its sub-detector systems and a person for scale. Retrieved from [4].

3.2.1 Coordinate System

The CMS experiment uses a right-handed coordinate system, with the origin at the nominal collision point, the x-axis pointing to the center of the LHC ring, the y-axis pointing up (perpendicular to the LHC plane), and the z-axis along the anticlockwise beam direction. The polar angle θ is measured from the positive z-axis and the azimuthal angle ϕ is measured from the positive x-axis in the $x-y$ plane. The radius r denotes the distance from the z-axis and the pseudorapidity η is defined as $\eta = -log[tan(\theta/2)]$. η is preferently used by CMS particle physicists to measure forward-ness of relativistic particles in the detector since any differences in this coordinate are invariant under boosts in the $z-$direction and particle production is roughly uniform in η. See Figure 3.3 for reference.

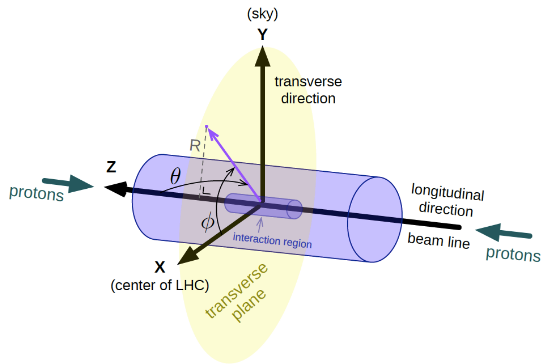

Figure 3.3: Diagram for the CMS detector coordinate system.

3.2.2 Solenoid

The CMS magnet[55] is one of the main features of the experiment. It delivers a 4T magnetic field, which is 100,000 times stronger than that of Earth over a length of 12.5 m and a free-bore radius of 3.15 m.

Its job is to bend the paths of charged particles emerging from high-energy collisions in the LHC. The higher momentum particles get their path curved less than the lighter ones, and as a result, curvature is an important tool for momentum measurements.

The strong magnetic field, combined with the high-precision position measurements in the tracker and muon detectors, allows for accurate measurement of the momentum of high-energy particles.

The CMS solenoid magnet is made of coils of wire that produce a uniform magnetic field when electricity flows through them.It is the largest superconducting magnet ever built, weighting about 12,000 tonnes. In order for it to be superconducting, it needs to be colled down to -268.5 C, which is a degree warmer than outer space.

The tracker and calorimeter detectors fit inside the magnet while the muon detectors are interleaved with a 12-sided iron structure that surrounds the magnet coils and contains and guides the field. Made up of three layers, this "return yoke" reaches out 14 meters in diameter and also acts as a filter, allowing through only muons and weakly interacting particles such as neutrinos. The enormous magnet also provides most of the experiment's structural support, and must be very strong itself to withstand the forces of its own magnetic field.

3.2.3 Tracker and Pixel Detector

The main purpose of the tracker sub-detector system is to reconstruct the trajectory of charged particles. Charged particles move in a helicoidal way which can be parameterized as a function of p_T, η, ϕ, z_0, and d_0. Here, z_0 and d_0 are the maximum longitudinal and transverse impact parameters relative to the centre of the beam spot, respectively. The beam spot is the luminous region produced by the collisions of proton beams.

As particles traverse the detector, they leave a ionization trail or *hits*. Without further analysis, it is not known which particle triggered which hits. Particle tracking consists in reconstructing the trajectories of the charged particles from the tracker measurements.

Momentum analysis in CMS makes use of the magnetic field provided by its super-conducting solenoid. The tracker sub-detector is not only able to measure the momentum of charged particles but also determines their direction at their production vertex.

A description of the hardware used for tracking is described in the following pharagraphs and the algorithms used for reconstructing and analyzing particle tracks can be found in Section 4.2.

The full sillicon inner tracking system[56] is a cylinder-shaped detector with an outer radius of 1.2 m and a length of 5.6 m. The barrel(each of the two endcaps) includes three(two) layers of pixel detectors, surrounded by ten(twelve) layers of micro-strip detectors. The 16,588 silicon sensor modules are finely segmented into 66 million 150×100 μm pixels and 9.6 million 80-to180 μm-wide strips. Figure 3.4 shows the layout of the tracker and its subsystems.

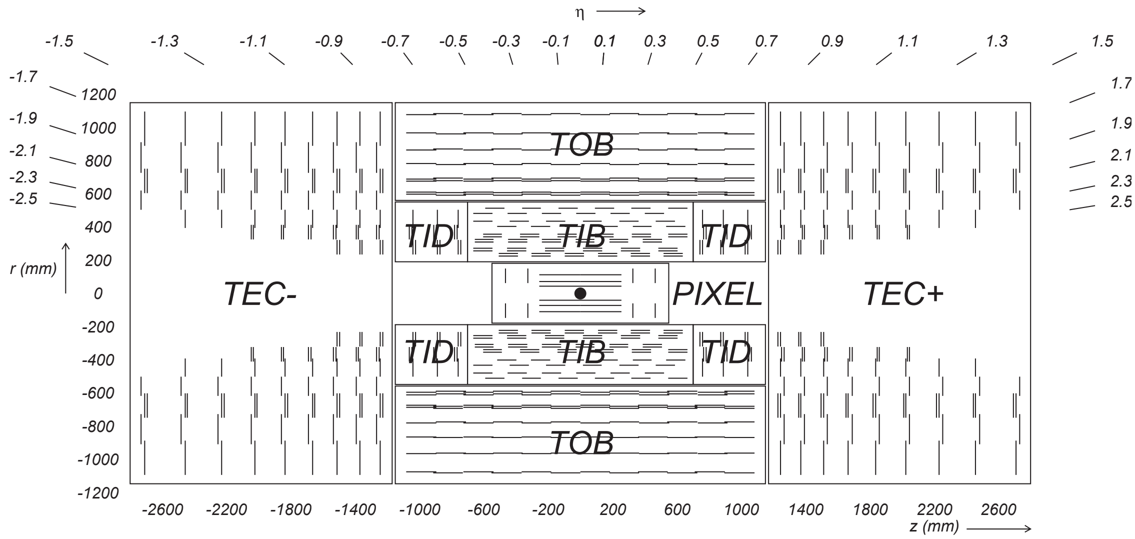

Figure 3.4: Layout of the CMS detector tracker with subsystems labeled.

The pixel detector is made up of three barrel layers, called BPIX, and two endcap layers called the FPIX. The BPIX contains 48 million pixels and the FPIX contains another 18 million pixels. In total it consists of 1440 hybrid silicon detector modules, each with a dimension of $100 \times 150 \mu m^2$. The small pixel size enables track resolutions of $10 \mu m$ in the transverse plane and $20 \mu m$ in the z-direction. The pixel detector is what gives CMS its excellent secondary vertex tagging ability in addition to producing seed tracks for the strip tracker and the high level trigger (HLT).

Likewise, the silicon strip detector is made up of four subsystems. The Tracker Inner Barrel (TIB) has four layers of 320 μm strips. At each end of the TIB is a three-layer Tracker Inner Disks (TID), which contains strips of the same thickness. The Tracker Outer Barrel (TOB) is the six layer system which surrounds the TIB/TID. The first four layers of the TOB use $500 \mu m$ thick strips, and the last two layers use 122 μm thick strips. The Tracker EndCaps (TEC) are on either side of the previous setup and contain nine disks with up to seven layers of strips. These strips are 320 μm thick in the inner four rings and 500 μm in the outer three rings. In total, the strip detector contains 9.3 million silicon strips.

The tracker measures the p_T of charged hadrons at normal incidence with a resolution of 1% for

$p_T < 20$ GeV[57]. The relative resolution then degrades with increasing p_T to reach the calorimeter energy resolution for track momenta of several hundred GeV.

3.2.4 Calorimeters

Calorimeters are an important class of detector used for measuring the energy and direction of a particle (or collection of particles) by its total absorption. They differ from most other detectors in that the nature of the particle is changed by the detector. Moreover, calorimeters can detecto both neutral and charged particles.

During the interaction with this type of detector, the particle will generate a cascade(s) of secondary particles by a process we will refer to as *showering*.

The absorption of a particle in a calorimeter is a statistical process governed by the Poisson distribution and therefore, the relative precision of energy measurements $\Delta E/E$ varies like $E^{-1/2}$ for large E.

Since the characteristics of electromagnetic and hadronic showers are somewhat different it is convenient to describe each subsystem separately.

3.2.4.1 Electromagnetic Calorimeter

Electromagnetic calorimeters are designed to measure the energy of electrons and photons. The CMS ECAL[58] is a homogeneous calorimeter made out of lead tungstate ($PbWO_4$) crystals totaling 75,848 units. The detector is divided up into two sections which provide a coverage of $|\eta| < 1.479$ in the barrel region (EB) and $1.479 < |\theta| < 3.0$ in two endcap regions (EE). There are also preshower detectors (PS) in each of the endcaps, in fornt of the EE, which cover a pseudorapidity range of $1.653 < |\eta| < 2.6$. Figure 3.5 shows the structure of the ECAL.

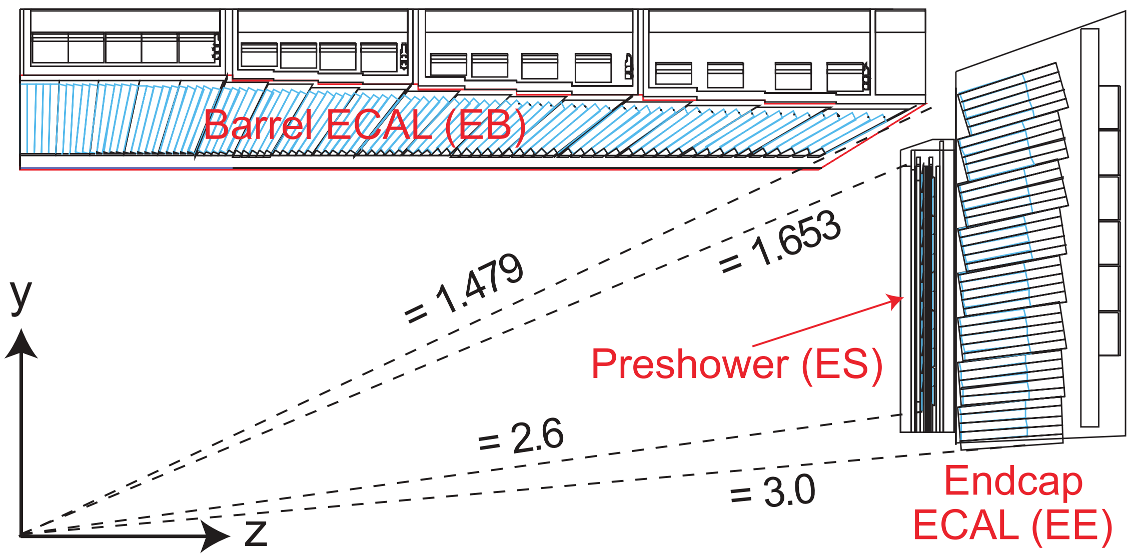

Figure 3.5: A schematic of the CMS ECAL detector with its subsystems labeled.

Each calorimeter cristal has a depth of 230 mm, which corresponds to 25.8 radiation lengths (X_0) for $PbWO_4$, sufficient to contain more than 98$\%$ of the energy of electrons and photont up to 1 TeV. The scintillation light produced in the crystals is read out by avalanche photodiodes (APDs), which produce approximately 4.5 photoelectrons per MeV at room temperature.

The crystal transverse size matches the small Moliére radius of $PbWO_4$, 2.2 cm. This fine transverse granularity makes it possible to fully resolve hadron and photon energy deposits as close as 5 cm from one another.

The intrinsic energy resolution (σ) of the ECAL barrel was measured with an ECAL supermodule directly exposed to an electron beam[59]. The relative energy resolution is typically parameterized as a function of the electron energy as

$$\frac{\sigma_E}{E} = \frac{2.8\%}{E[GeV]} \oplus \frac{12\%}{\sqrt{E[GeV]}} \oplus 0.3\% \tag{3.1}$$

3.2.4.2 *Hadron Calorimeter*

Hadronic calorimeters measure the energy of hadrons, as their name suggests. The CMS HCAL[60] is a sampling calorimeter, meaning it finds a particle's position, energy and arrival time using alternating layers of "absorber" and fluorescent scintillator or "active" materials that produce a rapid light pulse when the particle passes through.The produced light is then collected by optic fibers that feed it into readout boxes where photodetectors amplify the signal. The amount of light in a given region is summed up over many layers of tiles in depth, called a "tower".

The HCAL is organized into barrel (HB and HO), endcap (HE), and forward (HF). There are 36 barrel "wedges", each weighting 26 tonnes. These form the last layer of detector inside the magnetic coil. A few additional layers, the outer barrel (HO), sit outside the coil, ensuring no energy leaks out the back of the HB undetected. Similarly, 36 endcap wedges measure particle energies as they emerge through the ends of the solenoid magnet. In the barrel, the HCAL absorber thickness amounts to almost six interaction lengths at normal incidence, and increases to over ten interaction lengths at larger pseudorapidities. The HO material corresponds to 1.4 interaction lengths at normal incidence.

Lastly, the two hadronic forward calorimeters (HF) are positioned at either end of CMS, to detect particles coming out of the collision region at shallow angles relative to the beam line. These receive the bulk of the particle energy contained in the collision so must be very radiation resistant. Figure 3.6 shows the structure and position of the HCAL subsystems.

Combined, the ECAL and HCAL can measure the energy deposited by a charged pion with a resolution of $\sigma/E \approx 100\%/\sqrt{E[GeV]} \oplus 5\%$ [61], assuming an average jet particle composition.

3.2.5 Muon System

Since muons can penetrate several meters of iron without interacting, gas-ionization detector chambers were placed at the very edge of the experiment embedded in the steel flux-return yoke in order to detect them. This allows for a pseudorapidity coverage of $|\eta| < 2.4$.

The muon system consists of 1400 muon chambers which can be classified into three cate-

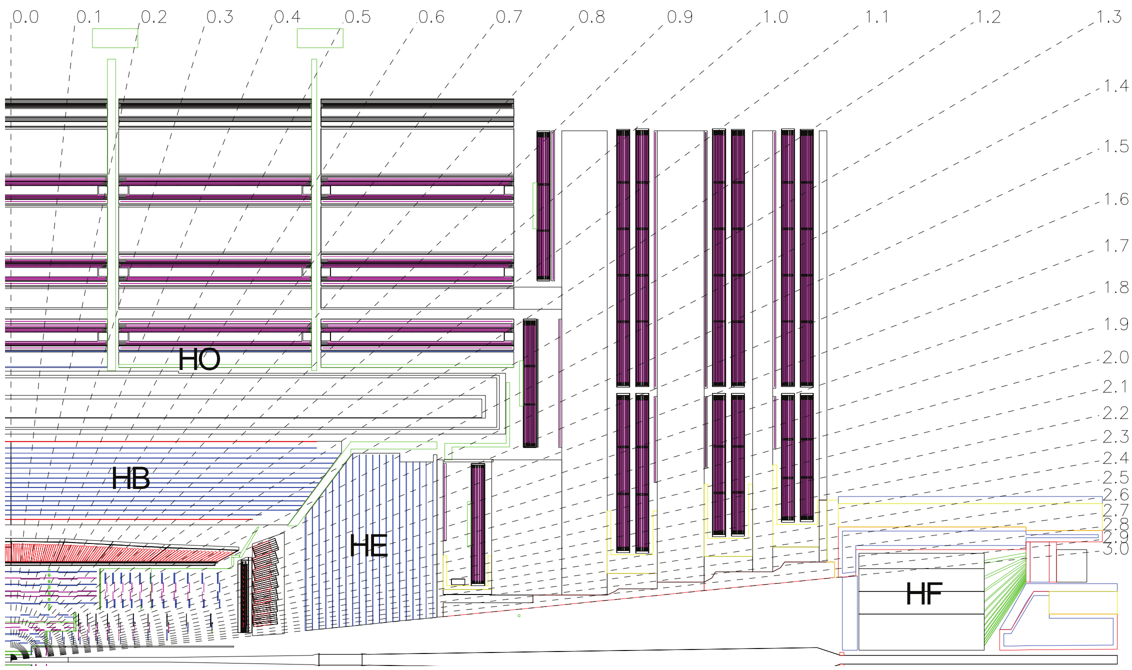

Figure 3.6: Structure and position of the CMS HCAL sub-detector systems.

gories, according to the technology used: 250 drift tubes (DTs), 540 cathode strip chambers(CSCs), and 610 resistive plate chambers(RPCs).

The barrel region of the detector contains DT's and RPCs, while the endcap region contains CSCs and RPCs. The layout of the muon system can be seen in Figure 3.7.

The four muon DT stations sitting outside the magnet coil are interleaved with the iron "return yoke" (shown in red in Figure 3.8, for the barrel region), which not only returns the flux from the solenoid, but also shields the muon chambers from hadrons.

The CSCs track the particle's position and allow for triggering, while the RPCs form a redundant trigger system, which quickly decides to keep the acquired muon data or not. Because of the many layers of detector and different specialties of each type, the system is naturally robust and able to filter out background noise.

The muon system on its own has a resolution of 15-40$\%$ depending on η. Matching muons to tracks measured in the silicon tracker results in a relative transverse momentum resolution for muons with 20$< p_T <$ 100 GeV of 1.3-2.0$\%$ in the barrel and better than 6$\%$ in the endcaps. The

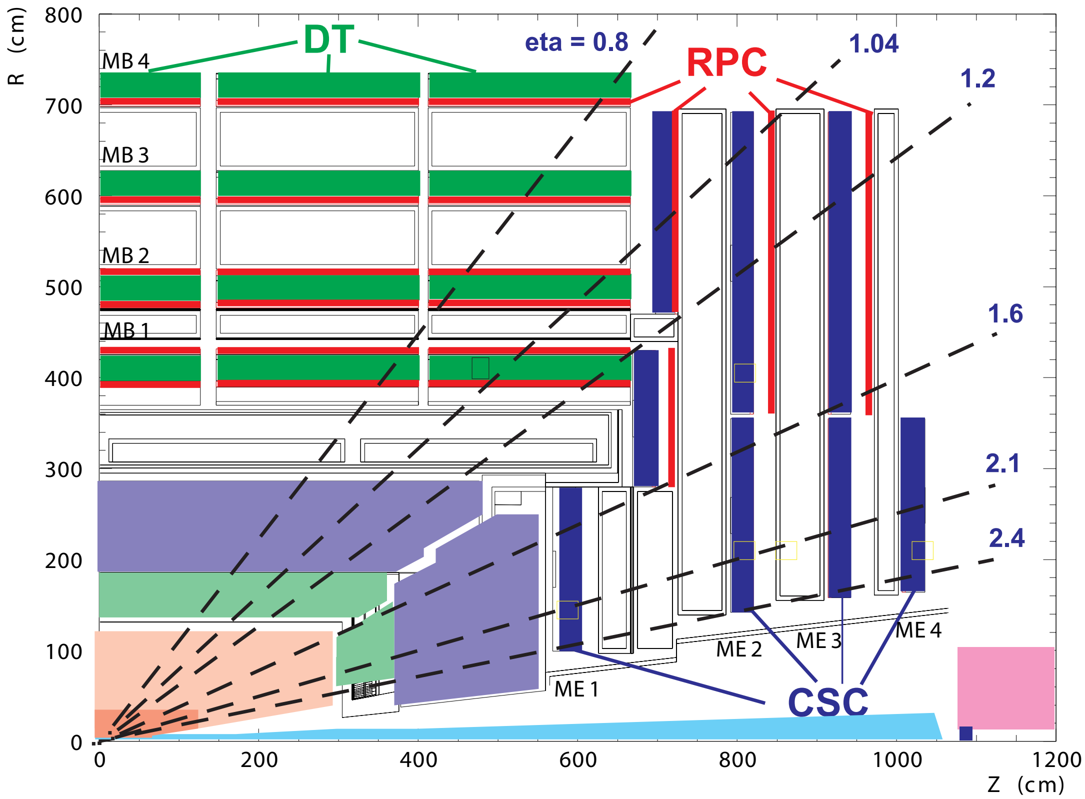

Figure 3.7: Layout of the CMS muon system.

p_T resolution in the barrel is better than 10% for muons up to 1 TeV [62].

3.2.6 Luminosity Measurement

Two important features of a particle accelerator are its center of mass energy and its instantaneous luminosity ($\mathcal{L}$). The lrgest the center of mass energy the more massive particles can be created and found, therefore, the largest the luminosity, the higher the chances of creating the particle.

Besides measuring the kinematics of each of the particles traversing the detector, CMS must also measure the instantaneous luminosity delivered by the LHC. Both the pixel detector, and the HF are able to measure the luminosity to varying degrees of accuracy.

For a given process, the number of interactions (N) is the product of $\mathcal{L}$ integrated over the data taking time period and the cross section for the process in question (σ_{ref}):

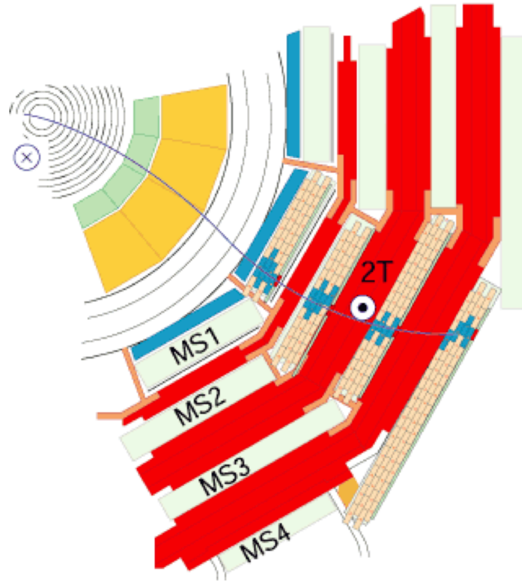

Figure 3.8: A muon, in the plane perpendicular to the LHC beams, leaves a curved trajectory in four layers of muon detectors or stations.

$$N = \sigma_{ref} \int \mathcal{L}(t)dt \tag{3.2}$$

The Van der Meer (VdM) scan method measures the size and shape of the interaction region of the colliding beams. This is achieved by displacing the beams in the x and y- (transverse) planes and measuring the relative interaction rates as a function of the transverse beam separation. For Gaussian beams, the luminosity as a function of the transverse displacement (δu) can then be expressed as:

$$\mathcal{L}(\delta u) = \mathcal{L}_0 exp[-\frac{\delta u^2}{2\sigma_u^2}] \tag{3.3}$$

where

$$\mathcal{L}_0 = \frac{N_1 N_2 f N_b}{2\pi\sqrt{(\sigma_{1x}^2 + \sigma_{2x}^2)(\sigma_{1y}^2 + \sigma_{2y}^2)}} \tag{3.4}$$

and $\sigma_u = \sqrt{\sigma_{1u}^2 + \sigma_{2x}^2}$ with $u = x, y$ for each separation plane, N_b the number of colliding bunches and f the revolution frequency.

A fit of the measured interaction rates as a function of the reparation will allow to determine the effective beam size as well as the maximum achievable collision rate ($\dot{N}$)

$$\dot{N} = \mathcal{L}\sigma \tag{3.5}$$

In practice, the scans are performed by moving the beams step-wise across each other in the two transverse plane.

During proton-proton collisions, interactions happen in a small longitudinal region near the center called the luminous region or interaction region. Collisions themselves are not recorded, only the particles that get created. The origin of one or more new particles is called a vertex. An event is the set of particle measurements in the detector associated to a single beam-beam crossing. It is the job of the reconstruction software to process the raw information and identify physics objects for a given event.

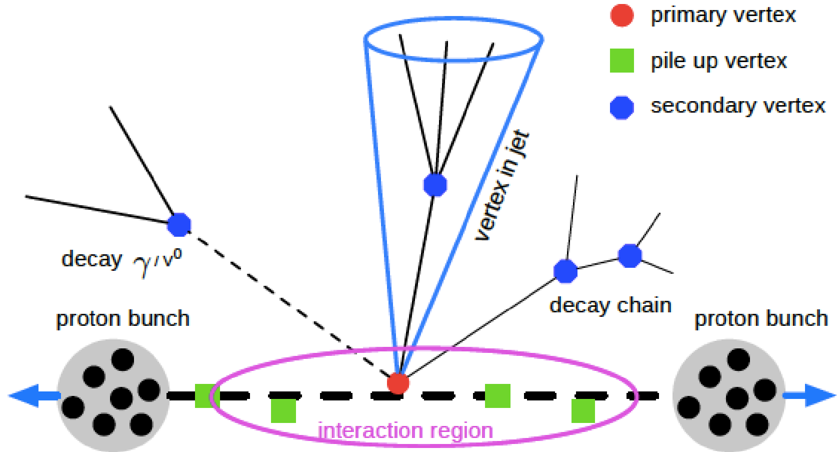

Figure 4.1: Schematic diagram for a reconstructed event at the LHC.

4.1 Data Acquisition

The CMS Data Acquisition (DAQ) and trigger system was specifically designed to collect and analyze data at a rate of 40MHz, which corresponds to a 25 ns collision rate. Unfortunately, it would be impossible to record all the acquired data and therefore only a small fraction of events are written to disk. Events filtering is performed online by the so-called trigger systems.

The collision triggering the readout is called the primary vertex, while other collisions from the beams are called pile-up. Secondary vertices refer to those production points where particles are created from decay or hard-scattering of the particles associated with a particular primary vertex. This is shown in Figure 4.1. Because higher energy collisions are more likely to produce something not yet seen, that makes them more interesting, so triggers are attuned to prefer higher momentum objects.

4.1.1 L1 Trigger and HLT

Whenever the LHC is performing at its peak, about one billion proton-proton interactions take place every second inside the CMS detector. To select events of potential physics interest, the CMS trigger[63] utilizes a two level system including a L1 hardware trigger and an HLT array of commercially available computers running high-level physics algorithms.

The first level (L1) of the CMS trigger is an extremely fast process that selects events containing candidate objects, e.g. ionization deposits consistent with a muon, or energy clusters consistent with an electron, photon, τ lepton, missing transverse energy (E_T^{miss}), or jet. In some cases, the scalar sum of the jet transverse momenta (H_T) is also used as a L1 candidate. During this process, only coarsely segmented data from calorimeter and muon detectors is used, while all the high-resolution data is held in pipeline memories in the front-end electronics.

The L1 trigger allows to store data for 3.2 μs, after which no more than 100 kHz of the stored events are forwarded to the next trigger system.

The event selection at the HLT is performed in a similar way to that used in the offline processing. For each event, objects such as electrons, muons, and jets are reconstructed and identification criteria are applied in order to select only those events which are of possible interest for data analysis.

The data processing of the HLT is structured around the concept of a *HLT path*, which is a set of algorithmic processing steps run in a predefined order that both reconstructs physics objects and makes selections on these objects.

The reconstruction modules and selection filters of the HLT use the software framework that is

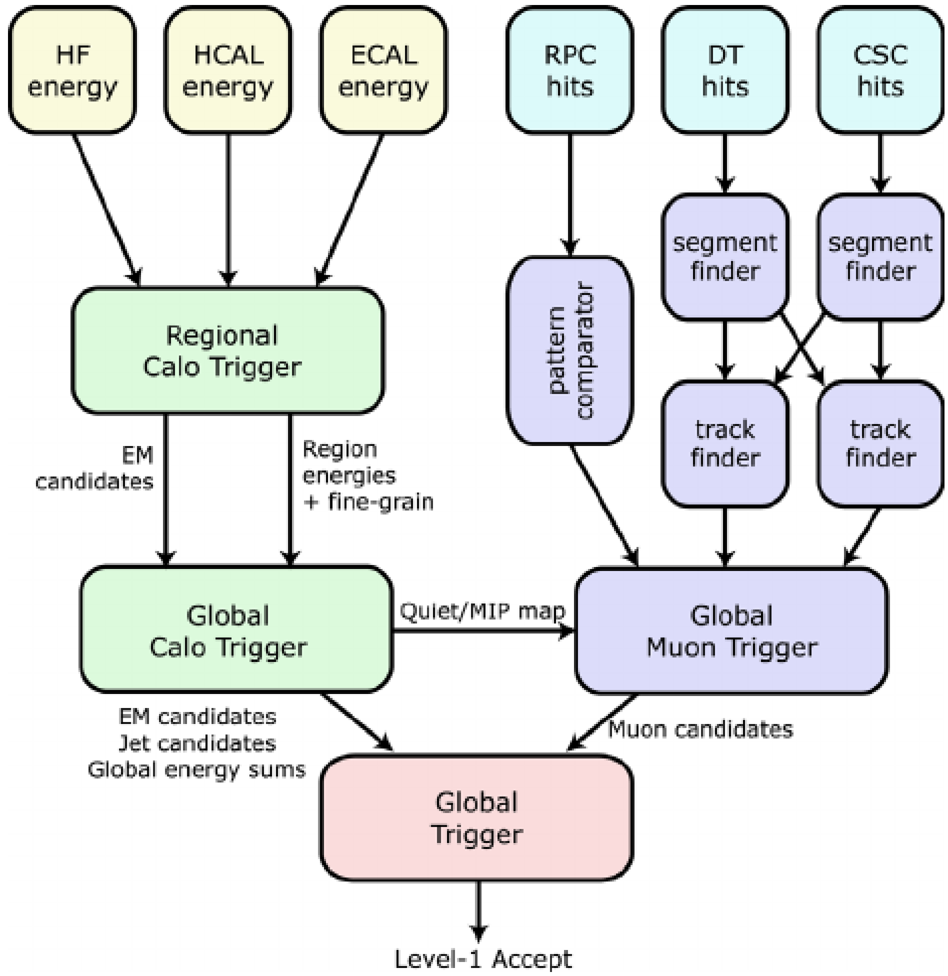

Figure 4.2: The CMS Level-1 Trigger. Reprinted from [64]

also used for offline reconstruction and analyses.

Upon completion, an average rate of 400 Hz of accepted events are sent to another software process, called the storage manager, for archival storage. The event data are stored locally on disk and eventually transferred to the CMS Tier-0 computing center for offline processing and permanent storage.

4.1.2 T1 sites and data storage

CMS computing operates on a tiered computing structure. A Tier-0 computing center is located at CERN where the data is transferred form the HLT and a first set of reconstruction occurs. From there, it is transferred to one of seven Tier-1 computing centers located around the world. At the

Tier-1 centers, a full reconstruction of the data is performed. Furthermore, there are 55 Tier-2 centers which can be accessed by the collaboration members for data processing and storage.

The analysis presented here was performed at one of the Tier-3 centers, the Texas A&M University Brazos HPC cluster.

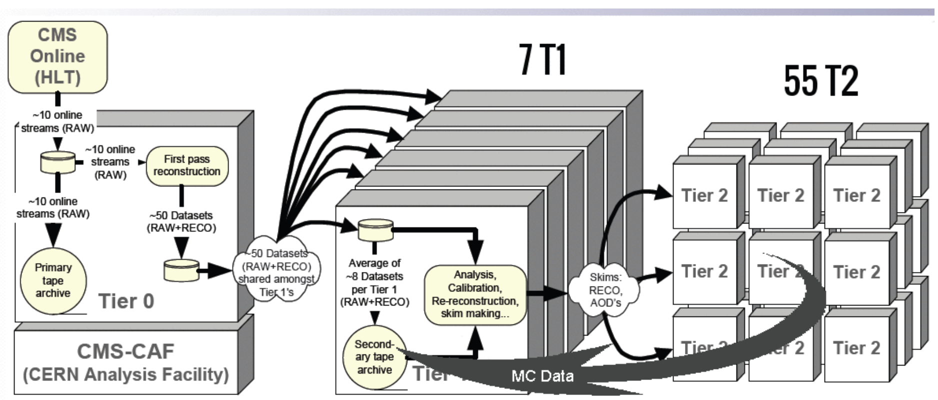

Figure 4.3: Flow of CMS detector data through the tiers. Reprinted from [5]

The data itself is also processed in three data tiers. The first layer of this is the RAW data, which is created by unpacking detector streams passed on from the L1 and HLT triggers. It is typically composed of measurements from the different subdetectors, as well as some information provided by the L1 trigger. RAW data is then reconstructed into PF objects, as explained in Section 4.2. This step is called RECO, which is short for reconstruction and contains both the detector and physics object information.

After the RECO step, an *analysis object data* (AOD) is generated from a subset of the RECO information. AOD objects are typically comprised of only high-level physics objects, making for much smaller files.

4.2 Particle Flow Event Reconstruction

In the previous section we described how data was managed and stored during the acquisition process. This section will focus on how raw detector information is interpreted.

First, detector data is measured in the form of electronic signals (hits in the tracker or energy depositions in the calorimeters). Then, the trajectories of charged particles, or tracks, are reconstructed from the position hits in the tracker. From the collection of tracks in an event, the primary and any secondary vertices are reconstructed.

An optimal event description can be achieved by correlating the basic elements from all subdetectors (tracks and clusters) to identify each final-state particle, and by combining the corresponding measurements to reconstruct the particle properties on the basis of this identification. At CMS, this approached is called *particle-flow (PF) reconstruction*.

The reconstructed and identified individual particle list includes muons, electrons, photons, as well as charged and neutral hadrons. These particles can be non-isolated, and even originate from an intricate overlap of reconstructed charged particles, ECAL and HCAL energy clusters, and signals in the muon chambers.

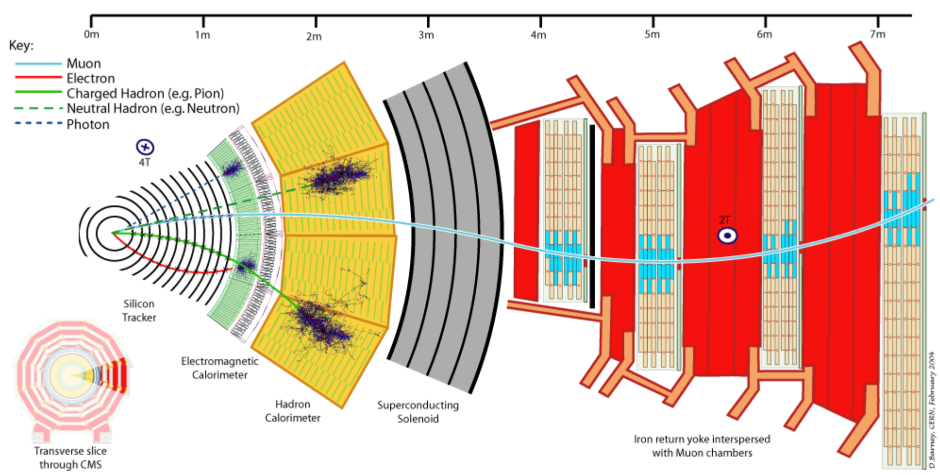

Figure 4.4: Cross-sectional view of the CMS detector with all of the sub-detectors labeled. The colored lines correspond to different particle types. Each particle interacts with different pieces of the detector and may or may not be bent by the magnetic field. Reprinted from [6]

During PF reconstruction, photons and neutral hadrons are identified by ECAL and HCAL clusters with no associated tracks. Electrons can be identified by associating a track to an ECAL cluster, with a momentum-to-energy ratio compatible with unity, and not connected to an HCAL cluster. Finally, muons and neutrinos would traverse the calorimeters with little or no interactions. While neutrinos would escape undetected, muons would be identified by a track in the inner tracker connected to a track in the muon detectors. See Figure **??**.

The PF concept was developed and used for the first time by the ALEPH experiment at LEP[65]. In particular, CMS is very well suited for PF reconstruction due to its highly-segmented tracker, a fine-grained ECAL, and an hermetic HCAL.

Also, the CMS magnet is large enough to accommodate the tracker and both the ECAL and HCAL, thereby minimizing the amount of material in front of the calorimeters. This particular feature is an advantage for PF reconstruction, as it eliminates the energy losses before the calorimeters caused by particles showering in the coil material and makes it easier to link tracks and calorimeter clusters.

4.2.1 Iterative Tracking

The first step of the PF reconstruction process consists of the reconstruction of hits in the pixel and strip tracker[66] and is referred to as local reconstruction.

The next step is track reconstruction, which refers to the process of using the reconstructed hits to obtain estimates for the momentum and position parameters of the charged particles responsible for the detector hits.

The tracking software at CMS[66] is commonly referred to as the combinatorial Track Finder (CTF), which is an adaptation of the combinatorial Kalman Filter [67, 68, 69], which in turn is an extension of the Kalman filter[70] to allow pattern recognition and track fitting to occur in the same framework. The collection of reconstructed tracks is produced by multiple passes or iterations of the same CTF track reconstruction sequence, in a process called iterative tracking.

The basic idea of iterative tracking is that tracks of relatively large p_T and those produced near the interaction region (which are relatively easy to find compare to those that are not) are searched for during the initial iteration. During successive iterations, hits associated with tracks discarded due to specific selection criteria are removed. By doing so, the combinatorial complexity is reduced, and subsequent iterations searching for more difficult types of tracks (e.g., low p_T, or greatly displaced tracks) is simplified.

Each iteration proceeds in four steps:

- Seed generation, which provides track candidates consisting of a few (2 or 3) hits. Seeds are generated in the innermost layers of the tracker and are commonly referred to as *proto-tracks*.

- Track finding, which is based on a Kalman filter. It extrapolates the seed trajectories along the expected flight path of a charged particle, searching for additional hits that can be assigned to the track candidate.

- Track fitting. A module that is used to provide the best possible estimate of the parameters of each trajectory by means of a Kalman filter.

- Track selection. This step sets the quality flags and discards tracks that fails certain specified criteria.

A total of six iterations are used, each with different seed generation, p_T, and impact parameter requirements. The first iterations follow a strict criterium in order to achieve a negligible small fake rate. Once the hits that are associated with so-called *fake tracks* are removed, the seeding criteria is loosened, and therefore, tracking efficiency is increased. From iteration 4 and on, the constraints on the tracks closer to the interaction point are slowly relaxed. This allows for reconstruction of secondary charged particles created from photon conversions and nuclear interactions in the tracker volume.

4.2.2 Calorimeter Clustering

Clustering in the calorimeters is the process of grouping detector cells that register hits together to measure the energy and direction of stable neutral particles. Additionally, clustering allows for a discrimination between neutral particles and energy deposits associated with charged hadrons; electron reconstruction, and a measurement of the energy of charged hadrons for which tracks were not determined accurately. The clustering algorithm is performed separately in each sub-detector: ECAL barrel and endcap, HCAL barrel and endcap, and in the pre-shower.

The clustering proceeds via three steps[71]:

1. Identify 'cluster seeds'. These are defined as the cell in a calorimeter with a local maximum of energy (above some set threshold).

2. Expand from the seed to grow 'topological clusters'. This is done by aggregating calorimeter cells that have at least one side in common with the seed cell, and also have an energy over a particular threshold.

3. Repeat the process of cluster growing, now using new cells that are part of the cluster.

In this sense, a "seed" gives rise to a "particle-flow cluster". If a cell is identified by two clusters, the energy is shared between the clusters according to the distance from the cell to the center of each cluster. The cluster energies and positions are iteratively determined as new cells are added to the cluster.

4.2.3 Linking Tracks and Clusters

Once the basic PF elements like the trajectories of charged particles in the inner tracker, electron and muon tracks, and calorimeter clusters are available, the next step in reconstructing a particle is the so-called *link algorithm*.

The link algorithm can test any pair of elements in the event. In order to prevent the computing time of the link algorithm from growing quadratically with the number of particles, the pairs of elements considered by the link procedure are restricted to the nearest neighbors in the (η, ϕ) plane, as obtained with a k-dimensional tree[72]. The specific conditions required to link two elements depend on their nature.

If two elements are found to be linked, the algorithm defines a distance between these two elements, aimed at quantifying the quality of the link. The link algorithm then produces *PF blocks* of elements associated either by a direct link or by an indirect link through common elements.

The link between tracks and calorimeter clusters proceeds by extrapolating the last measured hit in the tracker to one of the three detectors[71]:

- The two layers of the pre-shower detector,
- the ECAL, at a depth corresponding to the expected maximum of the electron shower profile,
- the HCAL, to a depth corresponding to one interaction length.

The track is then linked to a cluster in these detectors if the extrapolated position is within the cluster boundaries. Additionally, to link Bremsstrahlung photons to their associated electron, tangents to the track are extrapolated to the ECAL and any cluster found within those boundaries is also linked.

Similarly, links between the calorimeters are formed when a cluster from the more granular calorimeter (pre-shower or ECAL) is within the cluster envelope of the less granular calorimeter (ECAL or HCAL).

Finally, muon tracks are linked to charged particle tracks by a global fit between the two sets of tracks.

4.3 Physics Object Reconstruction

With the tracks identified, calorimeter clusters formed and the linking of clusters to tracks, particles can then be reconstructed. The PF process begins by reconstructing muons, then electrons and photons, and finally charged hadrons. As each particle is reconstructed, the tracks and clusters associated with it are removed from the collection of blocks used to form candidate particles, which ensures that energy deposits attributed to one particle are not used twice. The hadrons are then clustered together to form *jets*, and these jets can additionally be identified as coming from tau leptons or b quarks (Figure **??**).

4.4 Jets

During proton-proton collisions, the confined state of quarks and gluons is broken. Shortly after the collision, partons hadronize and a bunch of particles is generated by this process. These

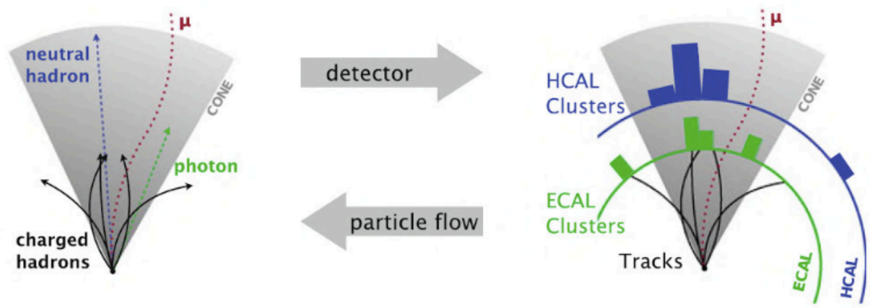

Figure 4.5: CMS Particle Flow algorithm. The diagram shows how collisions lead to particle decays and final state particles. On the right side of the diagram the tracks and deposits in the CMS detector are shown. The left side shows that PF candidates are derived from detector information and then become input for the PF algorithm that uses them to construct high-level physics objects like electrons, which are then used by analysts to reconstruct the collision event. Reprinted from [7]

particles are usually collimated in a given direction due to the boosted nature of the parton, and thereby produce a jet or spray of particles around it.

In practice, jets are the result of clustering groups of charged hadrons, photons, and neutral hadrons. The energy fraction in jets is divided amongst them with a breakdown of roughly 65%, 25%, and 10% respectively. This is illustrated in Figure **??**. For this study, jets were reconstructed from PF candidates clusters using the anti-k_T algorithm[9] as defined in the FASTJET package[73].

Jet clustering algorithms work by defining a distance parameter d_{ij} between PF candidates i and j and the distance between such cluster and the beam d_{iB}. These are defined as

$$d_{ij} = min(k_{ti}^{2p}, k_{tj}^{2p})\frac{\Delta_{ij}^2}{R^2} d_{iB} = k_{ti}^{2p} \tag{4.1}$$

where $\Delta_{ij}^2 = (y_i - y_j)^2 + (\phi_i - \phi_j)^2$, and k_{ti}, y_i, and ϕ_i are the transverse momentum, rapidity, and azimuth of particle i, respectively. R is a user-defined radius parameter, and p is a measure of the relative power of energy vs geometric scales. Particularly, for the anti-k_T algorithm, $p = -1$, and Equation 4.1 reduces to

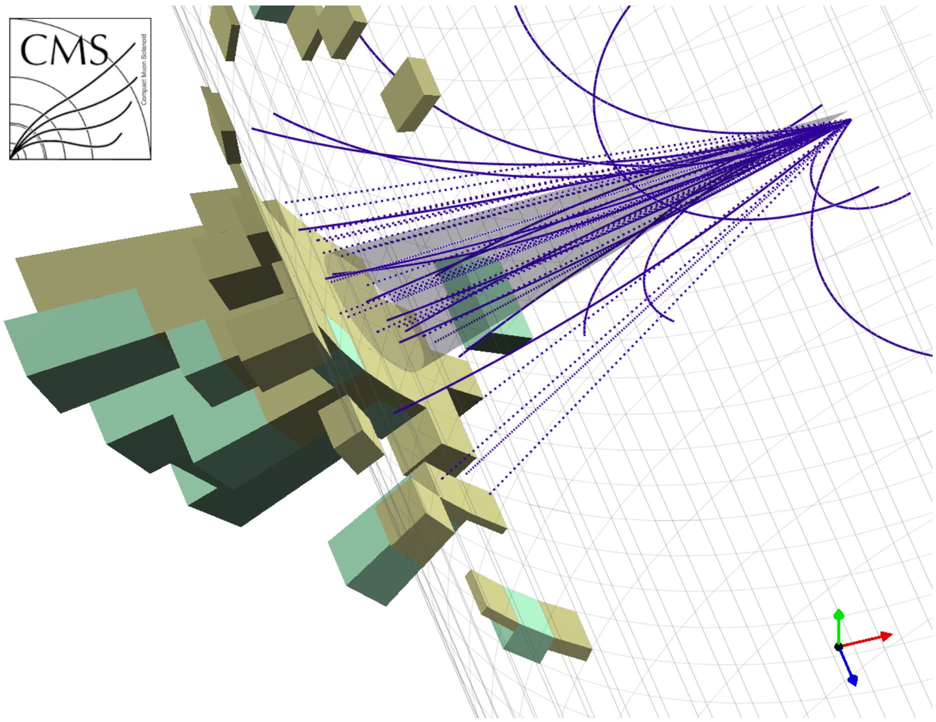

Figure 4.6: Schematic view of a jet with tracks and calorimeter deposits at CMS. Reprinted from [8]

$$d_{ij} = min(\frac{1}{p_{ti}^2}, \frac{1}{p_{tj}^2})\frac{\Delta_{ij}^2}{R^2} \tag{4.2}$$

The algorithm loops over all PF candidate objects, calculating d_{ij} for each pair of objects. Once it does this, it selects the two objects with the lowest value of d_{ij} and combines them. This process is repeated until the smallest value of d_{ij} satisfies the condition $d_{ij} > d_{iB}$.

As a result, the cutoff limit of $1/p_T^2$ defines a maximum size that the algorithm will look to cluster particles inside. The construction of d_{ij} using the inverse p_T^2 has a result of producing values of d_{ij} that are smaller for objects with a higher p_T, given equal separation. As a result, softer particles will tend to cluster to higher p_T particles long before they would cluster amongst themselves. If no hard particles are present, the jet object will simply cluster soft p_T particles in a circle in an $\eta - \phi$ space of radius R.

The clustering of the anti-k_T algorithm leads to jets with a large p_T being reconstructed as

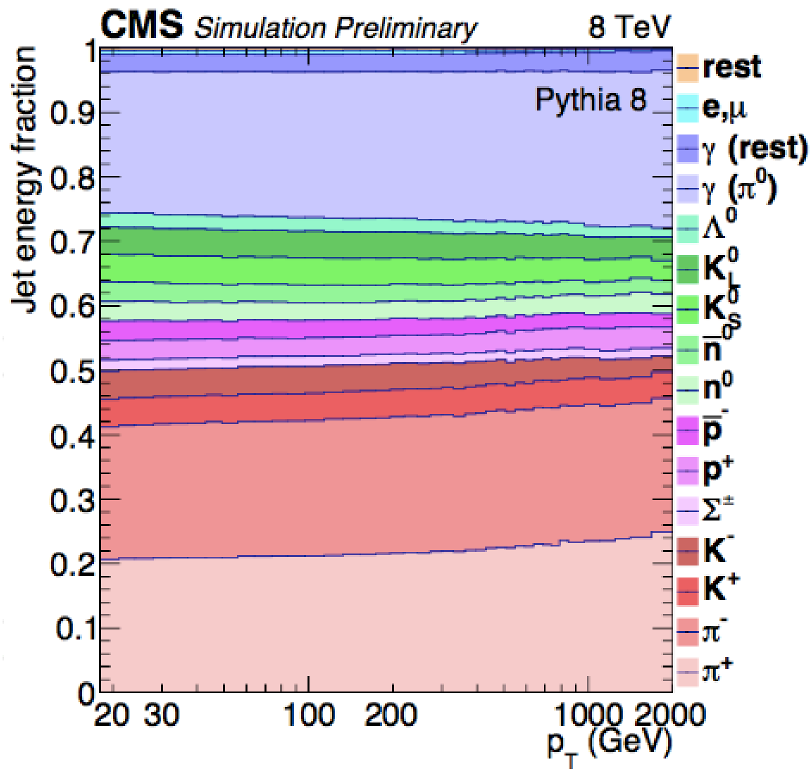

Figure 4.7: Particle composition for a jet. The energy fraction is relatively constant as a function of p_T^{jet} and corresponds to roughly 65%, 25%, and 10% charged hadrons, photons, and neutral hadrons, respectively. Reprinted from [9]

perfect circles, while softer jets can have a more ambiguous shape. Figure **??** shows a display of the anti-k_T algorithm for a distance parameter R=1. Notice that the green jet around $y = 2$ and $\phi = 5$ has a circular shape, while it deforms the smaller jet right next to it.

Finally, the anti-k_T algorithm is both infrared and collinear safe. Infrared safety implies that the jet clustering algorithm is insensitive to the emission of soft, wide angle particles. Under this condition, two jets would not be merged due to one of them producing a soft-momentum particle between them. Collinear safety means that if there is a splitting which results in two parallel high-p_T particles, a single jet is produced and the jet properties will not be different from a jet where this splitting did not occur. If the algorithm follows these two properties, it is referred to as being IRC safe.

The use of PF candidates, with their built in tracking information for jet reconstruction provides

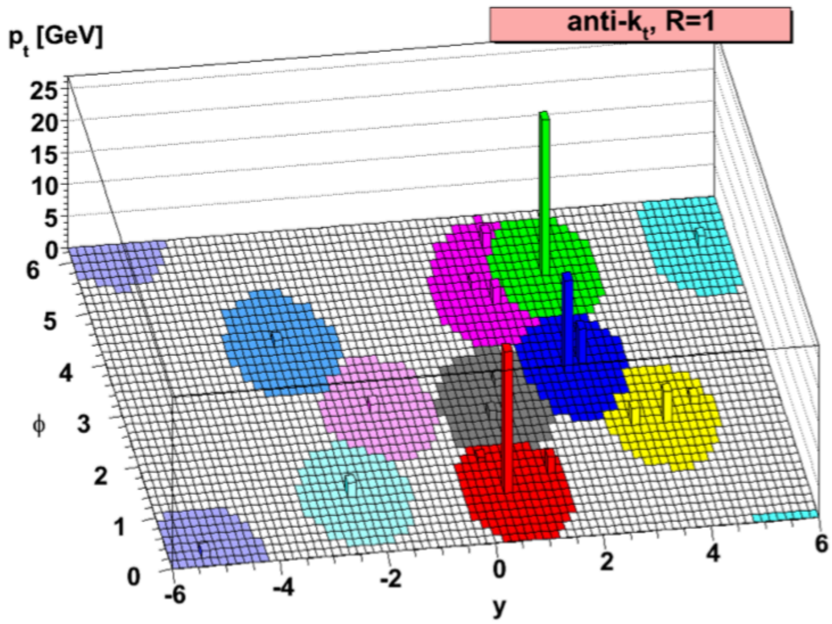

Figure 4.8: A sample parton-level event clustered with the anti-k_T algorithm. Reprinted from [9]

a jet resolution of 15% at 10 GeV, 8% at 100 GeV, and 4% at 1 TeV[7].

After the clustering procedure, the momentum and energy of the reconstructed jets still might not be the same as those from the initial parton, whether because of additional pileup energy produced during the same bunch crossing as the primary vertex or detector effects. To correct for this, CMS adopted a factorized approach[74], where each level of correction targets a specific effect and each correction factor obtained is applied in order. The goal is to make sure each jet has a relative response

$$\mathcal{R}_{rel} = \frac{p_T^{reco}}{p_T^{ref}} \tag{4.3}$$

as close as possible to unity. Here p_T^{reco} is the reconstructed jet p_T and p_T^{ref} is the true of reference p_T of the jet.

The process of correcting the jet 4-momentum by means of a scale or weight obtained from matching the reconstructed jet information to that of the reference jet in Monte Carlo is referred to as jet energy correction (JEC).

The first level of correction, commonly referred to as the L1FastJet[75] corrections, starts by removing pileup or electronic noise energy that may have made it into the jet reconstruction. This multiplicative correction will only remove energy from within the jet and will take the form in Equation 4.4, where ρ is the median energy density of the event, A is the jet area, and f is an estimate of the offset inside the jet per unit of jet area [74, 75].

$$p_T^{L1Corrected} = p_T^{uncorrected} \cdot (1 - A\frac{f(\eta, \rho, A)}{p_T^{uncorrected}}) \tag{4.4}$$

The L2Relative correction compensates for the nonlinearity in the jet response as a function of η while the L3Absolute correction does the same thing as a function of p_T. All three corrections are applied to both data and simulation. An additional level of correction, called L2L3Residual, is applied to data only in order to correct for the difference in scale between the data and simulation.

A final level of modification to the reconstructed objects is an η dependent smearing factor applied to the jet 4-momenta coming from the MC samples. The distribution of jet energies within the MC simulation tends to be more sharply peaked and less broad than the same distribution in data, resulting in a smaller jet energy resolution (JER) than we can realistically measure using the CMS detector. The deterministic "smearing" method recommended by CMS[76] matches the MC jet energy resolution to the one measured in data.

The reconstructed jet p_T is scaled by a correction factor C_{JER} as determined in Equation 4.5, where C_η is a correction factor derived as a function of η. The multiplicative JER correction factor is then used to modify the jet 4-momentum as in Equation 4.6.

$$C_{JER} = max\left(0.0, \frac{p_T^{GEN}}{p_T^{RECO}} + C_\eta \cdot \left(1 - \frac{p_T^{GEN}}{p_T^{RECO}}\right)\right) \tag{4.5}$$

$$\mathbf{X}_{Jet}^{corrected} = C_{JER} \cdot \mathbf{X}_{Jet}^{RECO} \tag{4.6}$$

A set of quality cuts, collectively called PF jet identification, are applied to the resulting collection of jets to ensure that only real, hard scatter PF jets are used during the analysis[77]. Several working point are defined at varying levels of efficiency and purity, but this analysis makes use of the tight criteria shown in Table 4.1[78].

Table 4.1: Cut based PF jet identification requirements for the tight working point.

Cut Variable	Cut Value		
	Tight		
η	$\|\eta\| \leq 2.7$	$2.7 < \|\eta\| \leq 3.0$	$\|\eta\| > 3.0$
Neutral Hadron Fraction	<0.90	<0.98	-
Neutral EM Fraction	<0.90	> 0.01	<0.90
$n_{constituents}$	>1	-	-
Muon fraction	<0.8	-	-
Number of Neutral Particles	-	> 2	>10
and for $\|\eta\| \leq 2.4$ in addition apply			
Charged Hadron Fraction	> 0		
Charged Multiplicity	> 0		
Charged EM Fraction	< 0.90		

All cuts on the jet energy fractions are made on the raw jets, before any energy correction is applied. In addition to the PF jet quality cuts, this analysis requires that all jets be within $|\eta| < 2.6$ and to have a $p_T > 30$ GeV.

4.5 b-tagging

Some jets are produced from a b-quark that after hadronization enters a bound state with another quatk and both become part of a B meson that has a long lifetime, and subsequently decay after it has traveled some distance. B-tagging is the identification of jets at some confidence level as having contained a B meson.

A variety of b-tagging algorithms has been developed by CMS to select b-quark jets[79] based on variables such as the impact parameters of the charged-particle tracks, the properties of reconstructed decay vertices, and the presence or absence of a lepton, or combinations thereof. These algorithms heavily rely on machine learning tools and are thus natural candidates for advanced tools

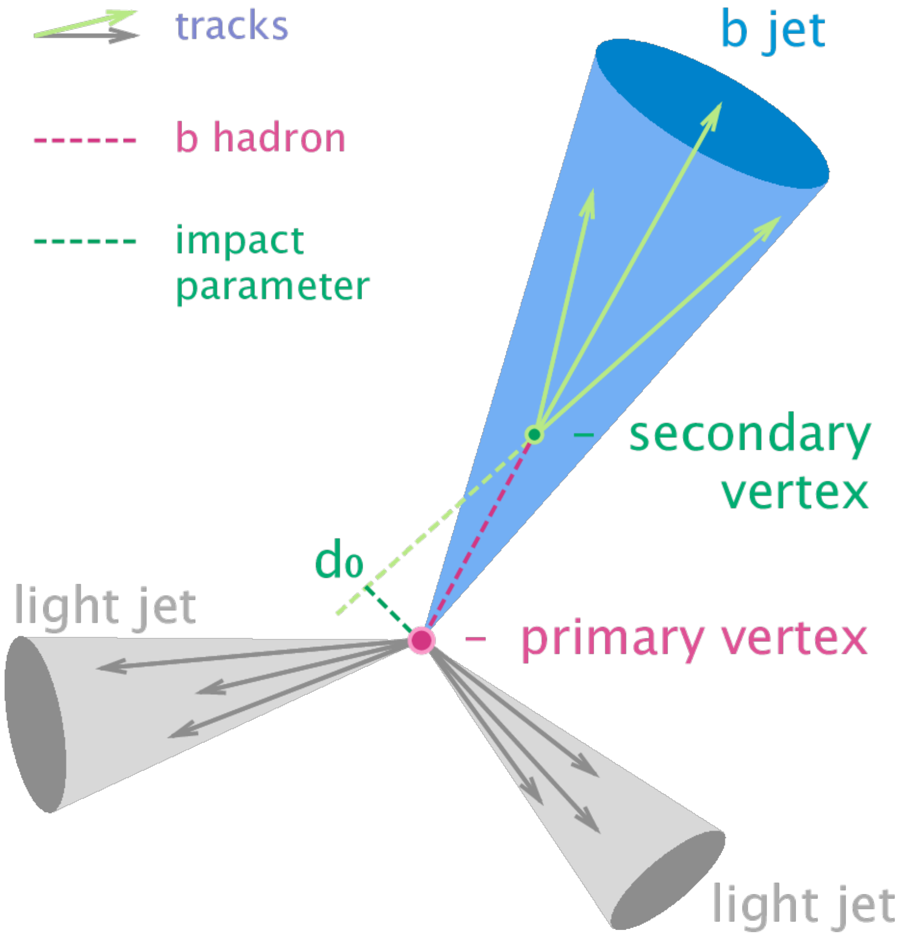

Figure 4.9: Diagram showing the common principle of identification of jets initiated by B hadron decays. Reprinted from [10]

like deep neural networks. In particular CMS makes use of a new algorithm, DeepCSV[11, 80], which uses a deep neural network trained using about 50 million simulated jets.

The DeepCVS algorithm uses the reconstructed tracks and secondary vertices found by using the *inclusive vertex finding* (IVF) algorithm [81]. The same input variables used for the CSVv2 tagger (Table 4.2 from [11]) are used, with the difference that the track-based variables use up to six tracks in the training of the DeepCSV. Jets are randomly selected in such a way that similar jet p_T and η distributions are obtained for all jet flavors. These distributions are also used as input variables in the training to take into account the correlation between the jet kinematics and the other variables. The distribution of all input variables is preprocessed to center the mean of each

Table 4.2: Input variables used for the CSVv2 algorithm.

Input variable
Secondary vertex 2D flight distance significance
Number of secondary vertices
Track η_{rel}
Corrected secondary vertex mass
Number of track from secondary vertex
Secondary vertex energy ratio
$\Delta R(Secondaryvertex, jet)$
3D interaction point significance of the first four tracks
Track $p_{T,rel}$
$\Delta R(track, jet)$
Track $p_{T,rel}$ ratio
Track distance
Track decay length
Summed tracks E_T ratio
ΔR(summed tracks, jet)
First track 2D interaction point significance above c threshold
Number of selected tracks
Jet p_T
Jet η

distribution around zero and to obtain a root-mean-square value of unity. All of the variables are presented to the multi-variable analysis (MVA) in the same way because of the preprocessing.

The training is performed using jets with p_T between 20 GeV and 1 TeV, and within the tracker acceptance. The relative ratio of jets of each flavor is set to 2:1:4 for b:c:udsg jets. a mixture of $t\bar{t}$ and multi-jet events is used to reduce the possible dependency of the training on the heavy-flavor quark production process.

The training of the deep neural network is performed using the KERAS[82] deep learning library, interfaced with the TENSORFLOW[83] library that is used for low-level operations such as convolutions. The neural network uses four hidden layers that are fully connected, each with 100 nodes. For the nodes in the last layer, a normalized exponential function is used for the activation to be able to interpret the output value as a probability for a certain jet flavor category, $P(f)$. The output layer contains five nodes corresponding to five jet flavor categories used in the training.

These categories are defined according to whether the jet contains exactly one b hadron, at least two b hadrons, exactly one c hadron and no b hadrons, at least two c hadrons and no b hadrons, or none of the aforementioned categories. Each of these categories is completely independent of the others, and the reasoning behind the chosen categorization has to do with the ability of identifying jets containing two b or c hadrons.

The tagger can categorize individual jets in so-called "Tight" (DeepCSVT), "Medium"(DeepCSVM), and "Loose"(DeepCSVL) categories or working points. These working points correspond to 0.1, 1, and 10 $\%$ misidentification rates, respectively.

Figure **??** shows the b-jet efficiency as a function of the jet p_T for the DeepCSV algorithm at different working points. These efficiencies are obtained on simulated $t\bar{t}$ events using jets within tracker acceptance with p_T > 30 GeV.

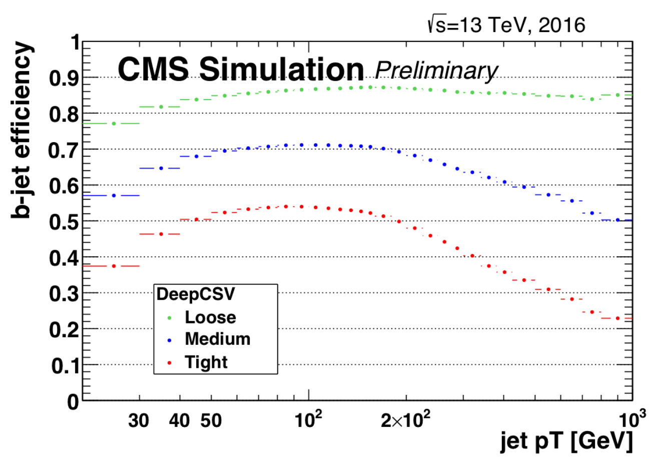

Figure 4.10: b-jet efficiency as a function of jet p_T for the DeepCSV algorithm for different working points. [11]

4.6 Event Generation

Searching for new physics can basically be reduced to a search for deviations from the SM. For this reason, extremely accurate signal and SM background predictions are required. For a given analysis, these predictions take the form of samples of events representing various physics scenarios, as they would be seen in the CMS detector. Monte Carlo (MC) event generators are used to simulate proton-proton collisions resulting in a variety of final states. The passage of these final states through the CMS detector is then simulated, and the resulting detector level data is analyzed. The reconstruction algorithms described in the previous section are then run on the simulated data, allowing for a direct comparison with real data.

4.6.1 Event Generators

Event generators are software packages which take a specific initial state as input and simulate all possible outcomes, or a selected subset of outcomes, from an interaction between the specified initial state particles. Bare partons produced in the hard scattering undergo gluon radiation or splitting, and subsequently undergo hadronization to form colorless hadrons. Unstable particles produced in the hard interaction or parton shower are made to decay to stable particles according to their known, or imposed, branching fractions and lifetimes.

During the event generation process, partons which take part in hard scattering interactions with large momentum transfer can be considered free due to asymptotic freedom. The large energy scale involved allows treatment of the interaction using perturbative methods. Under these assumptions, the proton-proton cross section at the LHC for a given N particle final state is given by

$$\sigma_N = \sum_{a,b} \int_0^1 dx_1 \int_0^1 dx_2 f_a(x_1, \mu^2) f_b(x_2, \mu^2) \hat{\sigma}_N^{ab} \tag{4.7}$$

where the sum is over all parton species a and b within protons 1 and 2. $f_i(x_j, \mu^2)$ is the probability (calculated at renormalization scale μ^2) of finding parton species i carrying a momentum fraction x_j of the parent proton j, and $\hat{\sigma}_N^{ab}$ is the partonic cross section for initial state $a + b$. The function $f_i(x_j, \mu^2)$ is referred to as a parton distribution function (PDF). The main task involved in simulation of the hard interaction is the evaluation of this integral. The partonic cross section is itself given by

$$\hat{\sigma}_N^{ab} = \int_{cuts} d\hat{\sigma}_N^{ab} = \frac{(2\pi)^4 S}{4\sqrt{(p_1 \cdot p_2)^2 - m_1^2 m_2^2}} \times \int_{cuts} \left[\prod_{i=1}^{N} \frac{d^3 q_i}{(2\pi)^3 2E_i} \right] \delta^4 \left(p_1 + p_2 - \sum_i^N q_i \right) |\mathcal{M}_{p_1 p_2 \to \{\vec{q}\}}^{ab}|^2 \tag{4.8}$$

where p_i are the incoming particle four-momenta, $q_i(E_i)$ are the outgoing particle four-momenta, S is a product of factors $1/j!$ for each set of j identical particles in the final state, and $\mathcal{M}_{p_1 p_2 \to \{\vec{q}\}}^{ab}$ is the parton level matrix element (ME) for the process. The event generator must build and evaluate all Feynman diagrams associated with the given process to determine the parton level ME, or these must be hard-coded by the package authors.

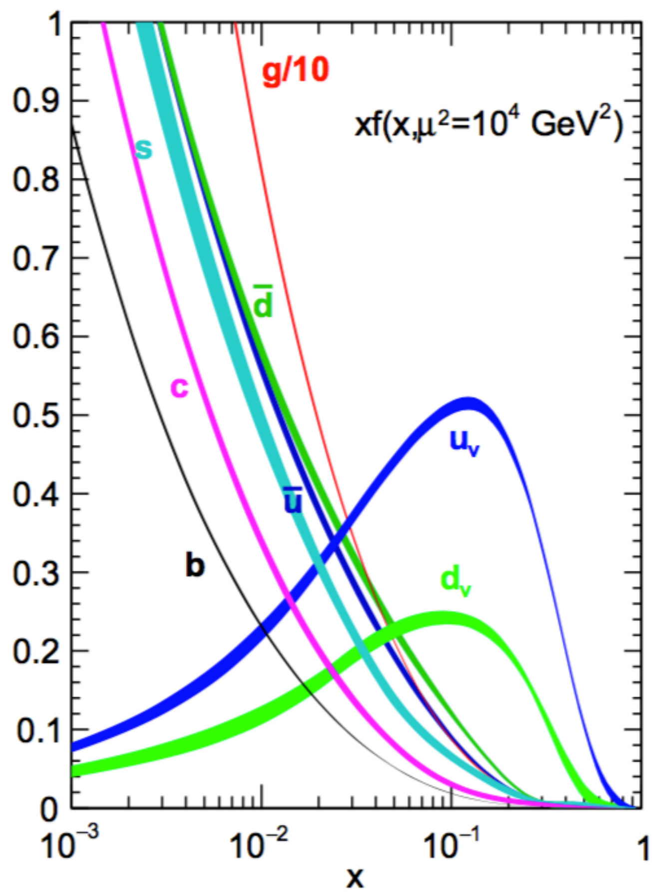

Figure 4.11: Parton distribution functions at the $\mu^2 = 10^4 GeV^2$ mass scale. Reprinted from [12]

The number of diagrams is directly proportional to the final state multiplicity and therefore becomes a complex problem very quickly. Next-to-leading-order (NLO) generators have recently been developed which include loop diagrams. This inclusion complicates the matter enormously as divergences arise in real and virtual contributions which must cancel.

Once the MEs have been evaluated, the evaluation of the multidimensional phase space integration required for the random sampling is performed using MC techniques. The spectator partons which did not take part in the initial hard interaction can undergo semi-hard interactions with each other, which is referred to as the underlying event (UE). Because these spectator interactions are typically soft, they are not calculable by perturbative methods and empirical models are used to describe them.

Bare partons may be produced as a result of the hard interaction. These partons are perturbatively evolved from the scale of the hard interaction through successive branchings down to a lower energy scale at which they combine to form colorless hadrons, the hadronization scale. These successive branchings are the origin of hadronic jets, whereby individual partons lead to a cascade of partons moving in the general direction of the original parton as they inherit its momentum. The probability for a parton to branch into two partons as it evolves from scale t to $t' < t$ and the kinematics of such a branching can ce calculated from first principles, accurate to fixed order in the strong coupling; the results of which are known as the DGLAP evolution equations[84]. Thus, the partons are recursively evolved down to the hadronization scale through successive branchings. After showering of an N-1 particle final state, an additional hard parton can be radiated, thus producing overlap with an N particle interaction hard state. The colored proton remnants which did not take part in the hard interaction can produce showers as well.

At the hadronization scale, the showering ceases and the colored partons group to form colorless hadrons. This regime is not amenable to perturbative calculations, and no first-principle theory is viable. Various phenomenological methods have been developed to model hadronization, including the *Lund-string-model*[85]. In the Lund model, color string attach to a pair of quarks, and as these strings stretch, energy is built up in the electromagnetic field until vacuum excitation of a quark-antiquark pair becomes possible. Ultimately, color connected pairs of quarks form hadrons.

The cluster hadronization model assumes a local parton-hadron duality, this hadronic quantum numbers result from the quantum numbers of local partons with minimal disruption needed to produce colorless hadrons. Regardless of the hadronization model choice, the produced hadrons are often unstable, and are then decayed to stable hadrons.

4.6.1.1 Pythia

PYTHIA[86] is a general purpose, tree level partonic matrix element generator capable of performing parton showering, hadronization, and UE simulation. A variety of $2 \rightarrow 1, 2, 3$ processes are included. Full spin correlations are included in the decays of unstable resonances. Shower evolution proceeds in terms of decreasing time-like virtuality, and imposes angular ordering by veto. Shower evolution is accurate to the LL level. The Lund string model is used for hadronization. UE interactions are described perturbatively as multiple nearly-independent $2 \rightarrow 2$ scatterings. PYTHIA 8 is used in this analysis to simulate signal samples with $xqcut = 30$ and $qcut = 60$.

4.6.1.2 MADGRAPH

MADGRAPH[87] is another generator that is used in this analysis for simulating hard parton emission (i.e. ISR and FSR), but must be interfaced with PYTHIA for showering and collinear radiation.

4.6.2 Detector Simulation

The next step in the simulation of events chain is the simulation of how particles will interact with the detector and its constituent materials and how the readout electronics will behave. To simulate the response of the CMS detector, the generators are interfaced with a sophisticated detector simulation based on the GEANT4[88] software package, which takes into account the exact detector geometry as well as all materials used.

The alignment, calibration, and other conditions which may change over time are periodically checked and stored in a database. These conditions are used for both offline simulation and reconstruction as well as for online activities. A snapshot of the conditions at some point in time is called a global tag. For reference, this analysis uses the $80X\_dataRun2\_2016LegacyRepro\_v4$ and $80X\_mcRun2\_asymptotic\_2016\_TrancheIV\_v8$ global tags for data and simulation, respectively.

The final state particles from the event generator are sent to the detector simulation, which tracks the particles as they move through the detector depositing energy into what are called simulated hits. While the models of electromagnetic interactions are extremely precise, the hadronic interactions have a greater uncertainty associated with them. The simulation goes through the data acquisition process, event simulating the responses of the photo detectors and readout electronics. The resulting information is then analyzed by the same reconstruction process that the real data goes through and is stored using the ROOT software library.

REFERENCES

[1] D. Dominguez, “Particles of the standard model of particle physics.” https://home.cern/science/physics/standard-model, 2016. [Online; accessed June 7, 2019.

[2] R. D. Ball *et al.*, “Parton distributions for the LHC Run II,” *JHEP*, vol. 04, p. 040, 2015.

[3] K. Andersen and T. Eberle, “The genesis 2.0 project.” http://media.vanityfair.com/photos/54cbf6ad1ca1cf0a23ac6c85/master/w_690,c_limit/image.jpg, 2010. [Online; accessed May 29, 2019.

[4] T. Sakuma, “A cutaway diagram of the cms detector.” https://en.wikipedia.org/wiki/Compact_Muon_Solenoid, 2013. [Online; accessed May 29, 2019.

[5] “Detector data flow through Hardware tiers.” https://twiki.cern.ch/twiki/bin/view/CMSPublic/WorkBookComputingModel, July 2018.

[6] “The CMS Detector and the Token Bit Manager.” https://www.phys.ksu.edu/reu2014/wabehn/, Jan 2017.

[7] “Particle-Flow Event Reconstruction in CMS and Performance for Jets, Taus, and MET,” Tech. Rep. CMS-PAS-PFT-09-001, CERN, Geneva, Apr 2009.

[8] Q. D. Blog, “Jets at cms.” https://www.quantumdiaries.org/2011/06/01/anatomy-of-a-jet-in-cms/, 2010. [Online; accessed June 27, 2019.

[9] M. Cacciari, G. P. Salam, and G. Soyez, “The anti-k_t jet clustering algorithm,” *JHEP*, vol. 04, p. 063, 2008.

[10] Wikipedia contributors, “B-tagging — Wikipedia, the free encyclopedia,” 2019. [Online; accessed 19-June-2019].

[11] T. C. Collaboration, “Identification of heavy-flavour jets with the CMS detector in pp collisions at 13 TeV,” *Journal of Instrumentation*, vol. 13, pp. P05011–P05011, may 2018.

[12] A. D. Martin, W. J. Stirling, R. S. Thorne, and G. Watt, "Parton distributions for the LHC," *Eur. Phys. J.*, vol. C63, pp. 189–285, 2009.

[13] G. Aad *et al.*, "Observation of a new particle in the search for the standard model higgs boson with the atlas detector at the lhc," *Physics Letters B*, vol. 716, no. 1, pp. 1 – 29, 2012.

[14] S. Chatrchyan *et al.*, "Observation of a new boson at a mass of 125 gev with the cms experiment at the lhc," *Physics Letters B*, vol. 716, no. 1, pp. 30 – 61, 2012.

[15] R. Aaij *et al.*, "Observation of $j\psi$ resonances consistent with pentaquark states in $\Lambda_b^0 \to j\psi K^- p$ decays," *Phys. Rev. Lett.*, vol. 115, p. 072001, Aug 2015.

[16] Wikipedia contributors, "Charge (physics) — Wikipedia, the free encyclopedia," 2019. [Online; accessed 7-June-2019].

[17] E. Noether, "Invariante variationsprobleme," *Nachrichten von der Gesellschaft der Wissenschaften zu Göttingen, Mathematisch-Physikalische Klasse*, vol. 1918, pp. 235–257, 1918.

[18] M. E. Peskin and D. V. Schroeder, *An Introduction to quantum field theory*. Reading, USA: Addison-Wesley, 1995.

[19] Wikipedia contributors, "Fermionic field — Wikipedia, the free encyclopedia," 2018. [Online; accessed 7-June-2019].

[20] Wikipedia contributors, "Gamma matrices — Wikipedia, the free encyclopedia," 2019. [Online; accessed 7-June-2019].

[21] G. Rajasekaran, "Fermi and the Theory of Weak Interactions," *Resonance J. Sci. Educ.*, vol. 19, no. 1, pp. 18–44, 2014.

[22] S. L. Glashow, "Partial Symmetries of Weak Interactions," *Nucl. Phys.*, vol. 22, pp. 579–588, 1961.

[23] S. Weinberg, "A model of leptons," *Phys. Rev. Lett.*, vol. 19, pp. 1264–1266, Nov 1967.

[24] A. Salam, "Weak and electromagnetic interactions," in *Elementary particle theory* (N. Svartholm, ed.), pp. 367–377, Almquist & Wiksell.

[25] J. Schwinger, “The theory of quantized fields. i,” *Phys. Rev.*, vol. 82, pp. 914–927, Jun 1951.

[26] T. P. Cheng and L. F. Li, *GAUGE THEORY OF ELEMENTARY PARTICLE PHYSICS*. 1984.

[27] B. Martin and G. Shaw, *Particle Physics*. Wiley, 2017.

[28] C. Patrignani *et al.*, “Review of Particle Physics,” *Chin. Phys.*, vol. C40, no. 10, p. 100001, 2016.

[29] The LHCb collaboration, “Differential branching fractions and isospin asymmetries of $b{\to}k^*\mu^+\mu$ decays,” *Journal of High Energy Physics*, vol. 2014, p. 133, Jun 2014.

[30] The LHCb collaboration, “Measurements of the s-wave fraction in $b^0{\to}k^+\pi\mu^+\mu$ decays and the $b^0{\to}k^{*0}(892)\mu^+\mu$ differential branching fraction,” *Journal of High Energy Physics*, vol. 2016, p. 47, Nov 2016.

[31] R. Aaij *et al.*, “Test of lepton universality using $B^+ \to K^+\ell^+\ell^-$ decays,” *Phys. Rev. Lett.*, vol. 113, p. 151601, Oct 2014.

[32] The LHCb collaboration, “Test of lepton universality with $b_0 \to k^{*0}l^+l$ decays,” *Journal of High Energy Physics*, vol. 2017, p. 55, Aug 2017.

[33] R. Aaij *et al.*, “Search for lepton-universality violation in $B^+ \to K^+\ell^+\ell^-$ decays,” *Phys. Rev. Lett.*, vol. 122, no. 19, p. 191801, 2019.

[34] R. Aaij *et al.*, “Measurement of form-factor-independent observables in the decay $B^0 \to K^{*0}\mu^+\mu^-$,” *Phys. Rev. Lett.*, vol. 111, p. 191801, Nov 2013.

[35] T. L. collaboration, “Angular analysis of the $B^0 \to K^{*0}\mu^+\mu^-$ decay using 3 fb1 of integrated luminosity,” *Journal of High Energy Physics*, vol. 2016, p. 104, Feb 2016.

[36] A. Abdesselam *et al.*, “Angular analysis of $B^0 \to K^*(892)^0\ell^+\ell^-$,” in *Proceedings, LHCSki 2016 - A First Discussion of 13 TeV Results: Obergurgl, Austria, April 10-15, 2016*, 2016.

[37] W. Altmannshofer, C. Niehoff, P. Stangl, and D. M. Straub, “Status of the $b \to k^*mu^+mu^-$ anomaly after moriond 2017,” *The European Physical Journal C*, vol. 77, p. 377, Jun 2017.

[38] M. Bordone, G. Isidori, and A. Pattori, "On the standard model predictions for r_K and r_{K^*}," *The European Physical Journal C*, vol. 76, p. 440, Aug 2016.

[39] G. D'Amico, M. Nardecchia, P. Panci, F. Sannino, A. Strumia, R. Torre, and A. Urbano, "Flavour anomalies after the rk measurement," *Journal of High Energy Physics*, vol. 2017, p. 10, Sep 2017.

[40] B. Capdevila, A. Crivellin, S. Descotes-Genon, J. Matias, and J. Virto, "Patterns of new physics in $b{\to}sll$ transitions in the light of recent data," *Journal of High Energy Physics*, vol. 2018, p. 93, Jan 2018.

[41] S. Bifani, S. Descotes-Genon, A. R. Vidal, and M.-H. Schune, "Review of lepton universality tests in b decays," *Journal of Physics G: Nuclear and Particle Physics*, vol. 46, p. 023001, dec 2018.

[42] F. Archilli, M. O. Bettler, P. Owen, and K. A. Petridis, "Flavour-changing neutral currents making and breaking the standard model," *Nature*, vol. 546, pp. 221 EP –, 06 2017.

[43] A. J. Buras and J. Girrbach, "Left-handed Z' and Z FCNC quark couplings facing new $b \to s\mu^+mu^-$ data," *J. High Energ. Phys.*, vol. 9, 2013.

[44] T. C. Collaboration, "Search for narrow resonances in dilepton mass spectra in proton-proton collisions at $\sqrt{s} = 13$ătev and combination with 8 tev data," *Physics Letters B*, vol. 768, pp. 57 – 80, 2017.

[45] A. M. Sirunyan *et al.*, "Search for high-mass resonances in dilepton final states in proton-proton collisions at $\sqrt{s} = 13$ TeV," *JHEP*, vol. 06, p. 120, 2018.

[46] T. A. Collaboration", "Search for new high-mass resonances in the dilepton final state using proton-proton collisions at $\sqrt{s}$ = 13 TeV with the ATLAS detector," Tech. Rep. ATLAS-CONF-2016-045, CERN, Geneva, Aug 2016.

[47] M. Abdullah, M. Dalchenko, B. Dutta, R. Eusebi, P. Huang, T. Kamon, D. Rathjens, and A. Thompson, "Bottom-quark fusion processes at the LHC for probing Z models and B -meson decay anomalies," *Phys. Rev.*, vol. D97, no. 7, p. 075035, 2018.

[48] W. Altmannshofer, P. Stangl, and D. M. Straub, "Interpreting hints for lepton flavor universality violation," *Phys. Rev. D*, vol. 96, p. 055008, Sep 2017.

[49] W. Altmannshofer, S. Gori, M. Pospelov, and I. Yavin, "Quark flavor transitions in $L_\mu - L_\tau$ models," *Phys. Rev. D*, vol. 89, p. 095033, May 2014.

[50] A. Breskin and R. Voss, *The CERN Large Hadron Collider: Accelerator and Experiments*. Geneva: CERN, 2009.

[51] S. Chatrchyan *et al.*, "The CMS experiment at the CERN LHC," *JINST*, vol. 3, p. S08004, 2008.

[52] G. Aad *et al.*, "The ATLAS Experiment at the CERN Large Hadron Collider," *Journal of Instrumentation*, vol. 3, no. 08, p. S08003, 2008.

[53] K. Aamodt *et al.*, "The ALICE experiment at the CERN LHC," *JINST*, vol. 3, p. S08002, 2008.

[54] A. A. Alves, Jr. *et al.*, "The LHCb Detector at the LHC," *JINST*, vol. 3, p. S08005, 2008.

[55] G. Acquistapace *et al.*, "CMS, the magnet project: Technical design report," 1997.

[56] C. collaboration, "The cms tracker: addendum to the technical design report," *CERN/LHCC*, vol. 16, 01 2000.

[57] T. C. Collaboration, "Particle-flow reconstruction and global event description with the CMS detector," *Journal of Instrumentation*, vol. 12, pp. P10003–P10003, oct 2017.

[58] *The CMS electromagnetic calorimeter project: Technical Design Report*. Technical Design Report CMS, Geneva: CERN, 1997.

[59] Q. Ingram, "Energy resolution of the barrel of the CMS electromagnetic calorimeter," *Journal of Instrumentation*, vol. 2, pp. P04004–P04004, apr 2007.

[60] "CMS: The hadron calorimeter technical design report," 1997.

[61] E. Yazgan and the CMS ECAL/HCAL Collaborations, "The CMS barrel calorimeter response to particle beams from 2 to 350 GeV/c," *Journal of Physics: Conference Series*, vol. 160, p. 012056, apr 2009.

[62] S. Chatrchyan *et al.*, "Performance of CMS muon reconstruction in pp collision events at $\sqrt{s} = 7TeV$," *JINST*, vol. 7, p. P10002, 2012.

[63] T. C. Collaboration, "The CMS trigger system," *Journal of Instrumentation*, vol. 12, pp. P01020–P01020, jan 2017.

[64] J. Brooke, D. Cussans, R. Frazier, G. Heath, D. Machin, D. Newbold, S. Galagadera, S. Madani, and A. Shah, "Hardware and firmware for the cms global calorimeter trigger," 07 2019.

[65] T. A. Collaboration, "Performance of the aleph detector at lep," *Nuclear Instruments and Methods in Physics Research Section A: Accelerators, Spectrometers, Detectors and Associated Equipment*, vol. 360, no. 3, pp. 481 – 506, 1995.

[66] S. Chatrchyan *et al.*, "Description and performance of track and primary-vertex reconstruction with the CMS tracker," *JINST*, vol. 9, p. P10009, 2014.

[67] P. Billoir, "Progressive track recognition with a Kalman like fitting procedure," *Comput. Phys. Commun.*, vol. 57, pp. 390–394, 1989.

[68] P. Billoir and S. Qian, "Simultaneous pattern recognition and track fitting by the kalman filtering method," *Nuclear Instruments and Methods in Physics Research Section A: Accelerators, Spectrometers, Detectors and Associated Equipment*, vol. 294, no. 1, pp. 219 – 228, 1990.

[69] R. Mankel, "A Concurrent track evolution algorithm for pattern recognition in the HERA-B main tracking system," *Nucl. Instrum. Meth.*, vol. A395, pp. 169–184, 1997.

[70] R. Fruhwirth, "Application of Kalman filtering to track and vertex fitting," *Nucl. Instrum. Meth.*, vol. A262, pp. 444–450, 1987.

[71] "Particle-Flow Event Reconstruction in CMS and Performance for Jets, Taus, and MET," 2009.

[72] J. L. Bentley, "Multidimensional binary search trees used for associative searching," *Commun. ACM*, vol. 18, pp. 509–517, 1975.

[73] M. Cacciari, G. P. Salam, and G. Soyez, "FastJet user manual," *Eur. Phys. J. C*, vol. 72, p. 1896, 2012.

[74] The CMS Collaboration, "Determination of jet energy calibration and transverse momentum resolution in cms," *Journal of Instrumentation*, 2011. http://iopscience.iop.org/1748-0221/6/11/P11002/.

[75] M. Cacciari and G. P. Salam, "Pileup subtraction using jet areas," *Physics Letters B*, 2008.

[76] "Jet Energy Resolution." `https://twiki.cern.ch/twiki/bin/viewauth/CMS/JetResolution`, 2017.

[77] N. Saoulidou, "Particle flow jet identification criteria," CMS Analysis Note CMS-AN-2010-003, CERN, Geneva, Jun 2010.

[78] "Jet identification." `https://twiki.cern.ch/twiki/bin/viewauth/CMS/JetID#Recommendations_for_13_TeV_2016`, 2018.

[79] S. Chatrchyan *et al.*, "Identification of b-quark jets with the CMS experiment," *JINST*, vol. 8, p. P04013, 2013.

[80] D. Guest, J. Collado, P. Baldi, S.-C. Hsu, G. Urban, and D. Whiteson, "Jet flavor classification in high-energy physics with deep neural networks," *Phys. Rev. D*, vol. 94, p. 112002, Dec 2016.

[81] W. Adam, "Track and vertex reconstruction in cms," *Nuclear Instruments and Methods in Physics Research Section A: Accelerators, Spectrometers, Detectors and Associated Equipment*, vol. 582, no. 3, pp. 781 – 784, 2007. VERTEX 2006.

[82] F. Chollet *et al.*, "Keras." `https://keras.io`, 2015.

[83] M. Abadi, A. Agarwal, P. Barham, E. Brevdo, Z. Chen, C. Citro, G. S. Corrado, A. Davis, J. Dean, M. Devin, S. Ghemawat, I. Goodfellow, A. Harp, G. Irving, M. Isard, Y. Jia, R. Jozefowicz, L. Kaiser, M. Kudlur, J. Levenberg, D. Mané, R. Monga, S. Moore, D. Murray, C. Olah, M. Schuster, J. Shlens, B. Steiner, I. Sutskever, K. Talwar, P. Tucker, V. Vanhoucke, V. Vasudevan, F. Viégas, O. Vinyals, P. Warden, M. Wattenberg, M. Wicke, Y. Yu, and X. Zheng, "TensorFlow: Large-scale machine learning on heterogeneous systems," 2015. Software available from tensorflow.org.

[84] G. Altarelli and G. Parisi, "Asymptotic Freedom in Parton Language," *Nucl. Phys.*, vol. B126, pp. 298–318, 1977.

[85] B. Andersson, G. Gustafson, G. Ingelman, and T. Sjöstrand, "Parton fragmentation and string dynamics," *Physics Reports*, vol. 97, no. 2, pp. 31 – 145, 1983.

[86] T. Sjöstrand, S. Ask, J. R. Christiansen, R. Corke, N. Desai, P. Ilten, S. Mrenna, S. Prestel, C. O. Rasmussen, and P. Z. Skands, "An Introduction to PYTHIA 8.2," *Comput. Phys. Commun.*, vol. 191, pp. 159–177, 2015.

[87] J. Alwall, C. Duhr, B. Fuks, O. Mattelaer, D. G. Öztürk, and C.-H. Shen, "Computing decay rates for new physics theories with FeynRules and MadGraph 5," *Comput. Phys. Commun.*, vol. 197, pp. 312–323. 29 p, Feb 2014. Comments: 29 pages, 2 figures.

[88] S. Agostinelli *et al.*, "Geant4 a simulation toolkit," *Nucl. Instrum. Meth. A*, vol. 506, no. 3, pp. 250 – 303, 2003.